nature communications

Article

https://doi.org/10.1038/s41467-024-55694-w

Divergent roles of m^{6}A in orchestrating brown and white adipocyte transcriptomes and systemic metabolism

Received: 22 February 2024

Accepted: 20 December 2024

Published online: 09 January 2025

Check for updates

Ling Xiao[1,7], Dario F. De Jesus[1,7], Cheng-Wei Ju[2,7], Jiang-Bo Wei[3], Jiang Hu[1], Ava DiStefano-Forti[1], Valeria Salerno Gonzales[1], Tadataka Tsuji[4], Siying Wei[5], Matthias Blüher[6], Yu-Hua Tseng[4], Chuan He[2] & Rohit N. Kulkarni[1]

N^6-methyladenosine (m^{6}A) is among the most abundant mRNA modifications, yet its cell-type-specific regulatory roles remain unclear. Here we show that m^{6}A methyltransferase-like 14 (METTL14) differentially regulates transcriptome in brown versus white adipose tissue (BAT and WAT), leading to divergent metabolic outcomes. In humans and mice with insulin resistance, METTL14 expression differs significantly from BAT and WAT in the context of its correlation with insulin sensitivity. *Mettl14*-knockout in BAT promotes prostaglandin secretion, improving systemic insulin sensitivity. Conversely, *Mettl14*-knockout in WAT triggers adipocyte apoptosis and systemic insulin resistance. m^{6}A-seq and RNA-seq integration revealed upregulated prostaglandin biosynthesis pathways in BAT and apoptotic pathways in WAT with *Mettl14* deficiency. Stable *METTL14*-knockout hBAs/hWAs show METTL14-mediated m^{6}A promotes mRNA decay of *PTGES2* and *CBR1* in hBAs and *TRAIL* and *TNFR1* in hWAs. These data shed light on the ability of m^{6}A to impact metabolism in a cell-type-specific manner with implications for influencing the pathophysiology of metabolic diseases.

N^6-methyladenosine (m^{6}A) modification is a pivotal post-transcriptional regulatory process in mammalian cells, controlled by writers (METTL3, METTL14, WTAP), erasers (ALKBH5, FTO), and readers (YTHDC, YTHDF, IGF2BP2)[1,2]. m^{6}A methylation of mRNA can affect its expression, stability, and translation efficiency, leading to altered protein abundance to determine diverse biological outcomes related to cell fate determination, organ development, cell proliferation, and/or survival[1,2]. Indeed, this ability to modify mRNA to regulate intricate cell processes can be an advantage considering the human body comprises more than 200 distinct cell types, each with specialized roles in physiological processes. Nevertheless, m^{6}A has also shown divergent functions; for example, METTL14-mediated m^{6}A modification exhibits both oncogenic[3–5] and anti-tumor effects[6,7] across cancer types. A lingering question in the field of m^{6}A biology pertains to the precise molecular underpinnings by which m^{6}A governs cell-type-specific modulation of gene expression in a contingent fashion, thereby affording precise control over diverse cellular functionalities. Therefore, understanding cell-type-specific m^{6}A regulation is crucial for unraveling the complexities of cellular processes and for developing targeted therapeutic strategies for various pathophysiological states including metabolic diseases[8].

[1]Section of Islet Cell and Regenerative Biology, Joslin Diabetes Center; Department of Medicine, BIDMC; Harvard Stem Cell Institute, Harvard Medical School, Boston, MA, USA. [2]Department of Chemistry, Howard Hughes Medical Institute, The University of Chicago, Chicago, USA. [3]Department of Chemistry, National University of Singapore, Singapore, Singapore. [4]Section on Integrative Physiology and Metabolism, Joslin Diabetes Center; Department of Medicine, BIDMC, Harvard Medical School; Harvard Stem Cell Institute, Boston, MA, USA. [5]Section of Islet Cell and Regenerative Biology, and CRISPR Screen Core Laboratory, Joslin Diabetes Center; Department of Medicine, BIDMC; Harvard Medical School, Boston, MA, USA. [6]Helmholtz Institute for Metabolic, Obesity and Vascular Research, HI Leipzig, Germany. [7]These authors contributed equally: Ling Xiao, Dario F. De Jesus, Cheng-Wei Ju. e-mail: Rohit.Kulkarni@joslin.harvard.edu

Brown adipose tissue (BAT) and white adipose tissue (WAT) are two major types of tissues that share some common features but also have distinct properties. BAT is specialized for energy expenditure through thermogenesis and is acknowledged as a secretory organ capable of producing various batokines that play roles in energy metabolism, inflammation, and/or whole-body insulin sensitivity[9,10]. WAT primarily functions as an energy storage depot, accumulating excess energy in the form of triglycerides (TGs)[9,11,12]. In addition, WAT also secretes endocrine hormones that can regulate the metabolism of distal organs. Dysregulation of WAT, specifically in the context of perturbed signaling pathways involving cytokines of the tumor necrosis factor (TNF) family, underlies the initiation of cellular apoptosis and inflammation within the adipose tissue, eventually resulting in lipid spill-over, glucotoxicity, and insulin resistance[13]. Hence, the context-specific regulation within distinct cell types such as BAT and WAT holds relevance for the modulation of whole-body metabolism.

The involvement of m^{6}A modification in BAT and WAT has recently emerged as a nascent yet critical realm of investigation, particularly within the scope of addressing obesity and metabolic disorders. While METTL3, METTL14, and WTAP are classified as major components of the m^{6}A writer complex, previous research including our own argues for unique roles for each. Some studies have investigated the impact of m^{6}A by focusing on METTL3 and WTAP on adipose tissue biology and function, with a particular focus on BAT or beige adipocytes[14–18]. Our previous study indicates that *Mettl14* deficiency in BAT promotes the secretion of beneficial endocrine factor(s) to protect mice from diet-induced obesity (DIO) and insulin resistance independent of BAT thermogenesis[19]. In this manuscript, we directly address the cell-type specific regulation involving m^{6}A by examining the roles of METTL14 in BAT versus WAT in the modulation of whole-body metabolism.

In this study, we build on our preliminary observations of distinct expression patterns of METTL14 in BAT versus WAT from humans and mice with insulin resistance. The BAT-specific (*Ucp1*-cre-driven) *Mettl14*-knockout (M14^{KO}) mouse model exhibits enhanced secretion of endocrine factor(s) with improved systemic metabolic homeostasis that is independent of BAT thermogenic function. Conversely, an independent mouse model with *Adipoq*-cre-driven *Mettl14*-knockout shows white adipocyte apoptosis that consequently reduces its lipid storage capacity, impairing whole-body insulin sensitivity and energy expenditure. m^{6}A-MeRIP-sequencing (m^{6}A-seq) and RNA-sequencing (RNA-seq) in *Mettl14*-deficient BAT versus *Mettl14*-deficient WAT revealed different methylomes and transcriptomes in the two cell types. Mechanistically, Mettl14-mediated m^{6}A modification specifically destabilizes critical BAT transcripts associated with phospholipid metabolic processes, while in WAT, it negatively regulates TNFα and apoptosis pathway-related genes via m^{6}A-dependent and independent mechanisms. These findings underscore the divergent roles of METTL14 in BAT versus WAT-mediated metabolism, emphasizing cell-type and context-specific m^{6}A regulation as a significant consideration for addressing metabolic disorders.

Results

Differential abundance of METTL14 in BAT versus WAT obtained from humans or mice with insulin resistance

To distinguish the m^{6}A methylome landscapes between BAT and WAT, we compared RNA-seq and m^{6}A-MeRIP-seq analyses between fully differentiated human brown adipocytes (hBAs) versus human white adipocytes (hWAs)[20]. To substantiate that m^{6}A selectively modifies transcripts expressed in hBAs and hWAs, we first filtered the transcripts unique to hWAs or hBAs and identified 25,563 transcripts that were ubiquitously expressed in both cell types (Supplementary Fig. 1a). Next, to specifically focus on the m^{6}A-modified transcripts, we intersected these 25,563 transcripts with those that are m^{6}A-modified, to reveal a total of 7866 m^{6}A-modified transcripts (Supplementary Fig. 1b). Principal component analysis (PCA) of the m^{6}A-seq data revealed a distinct separation between hBAs and hWAs (Supplementary Fig. 1c). About a quarter (2086) of the 7866 m^{6}A-modified transcripts showed comparable m^{6}A methylation levels between hBAs and hWAs (Supplementary Fig. 1d). On the other hand, 2681 and 3099 hypermethylated m^{6}A transcripts were exclusively identified in hBAs and hWAs, respectively (Supplementary Fig. 1d). These differentially m^{6}A-modified transcripts were notably enriched in pathways associated with VEGFA-VEGFR2, TGFβ, mRNA processing, insulin, TNFα, or apoptosis modulation signaling pathways (Supplementary Fig. 1e). Thus, brown and white adipocytes manifest highly distinct m^{6}A modification patterns that strongly align with cell-type-specific gene expression programs, pointing to functional specificity of m^{6}A at the cellular/tissue level. These preliminary results provided us with the rationale to explore the direct impact of m^{6}A modulators in these two different metabolic cell types.

METTL14, as a key component of the m^{6}A writer complex, has been reported to exhibit pronounced cell-type-specific roles within the context of metabolism[19,21]. For example, our previous studies revealed that m^{6}A hypomethylation, and more specifically *METTL14* downregulation, led to impaired β-cell function and identity[21]. Conversely, *METTL14* showed higher gene expression in BAT from humans with obesity, and BAT-specific *Mettl14*-knockout mice presented improved systemic insulin sensitivity[19]. Considering these observations, we hypothesized that METTL14 has divergent roles in the transcriptional programs to regulate the functions of brown versus white adipocytes.

To investigate this hypothesis, we first examined METTL14 protein abundance in the fully differentiated hBAs and hWAs under physiological conditions. We observed a higher relative METTL14 protein level in hWAs compared to hBAs cells (Supplementary Fig. 1f, g). In C57BL/6 N male mice fed a chow diet (CD), METTL14 protein abundance was significantly higher in inguinal white adipose tissue (iWAT) than epididymal white adipose tissue (eWAT) or interscapular brown adipose tissue (iBAT) (Supplementary Fig. 1h, i). These data support the notion that METTL14 exhibits adipocyte- and adipose depot-specific expression patterns under physiological conditions.

Next, we examined whether METTL14 exhibits differential expression across distinct human WATs, such as individuals with varying levels of body mass index (BMI) or insulin sensitivity (Supplementary Table 1). First, a comparison between lean, insulin-sensitive individuals and those with obesity but who are also insulin-sensitive revealed no significant differences in METTL14 protein abundance (Supplementary Fig. 1j, k). Likewise, when comparing individuals who are lean and insulin-resistant to those with obesity and insulin-resistant, no significant differences were detected in the levels of METTL14 protein (Supplementary Fig. 1l, m). This lack of distinction may be attributable to patient heterogeneity and it is possible that METTL14 abundance is not intrinsically linked to human BMI.

Next, to isolate the influence of insulin sensitivity from BMI, we compared individuals with obesity who are insulin-sensitive (HOMA-IR < 2.9) to individuals with obesity who are insulin-resistant (HOMA-IR > 2.9). Remarkably, METTL14 protein level was significantly lower in both subcutaneous white adipose tissue (scWAT) and visceral white adipose tissue (vsWAT) from humans with insulin resistance (Fig. 1a, b). Spearman correlation analysis revealed a robust negative correlation between METTL14 abundance and HOMA-IR in scWAT or vcWAT (Fig. 1c, d).

Consistent with the human data we detected similar changes in three different mouse models. First, we examined METTL14 protein levels in the fat tissues from the *ob/ob* (Lep^{ob}) mouse, which is a model for T2D and obesity that is characterized by hyperinsulinemia (Supplementary Fig. 1n), glucose intolerance (Supplementary Fig. 1o), and insulin resistance (Supplementary Fig. 1p). The METTL14 protein levels were lower in iWAT and eWAT from *ob/ob* mice compared to *ob*+ mice (Fig. 1e, f). On the other hand, the METTL14

https://doi.org/10.1038/s41467-024-55694-w

protein level was higher in the *ob/ob*-iBAT as compared to *ob/+*-iBAT (Fig. 1e, f). Thus, in the *ob/ob* mouse model, METTL14 in WATs is positively correlated with insulin sensitivity, and its protein abundance in BAT is negatively correlated with insulin sensitivity (Fig. 1g–i). In the *db/db* ($Lepr^{db}$) mouse model, which exhibits hyperinsulinemia (Supplementary Fig. 1q) and peripheral tissue insulin resistance (Supplementary Fig. 1r), METTL14 protein level was lower in iWAT and eWAT as compared to the *db+* controls (Fig. 1j, k). Conversely, elevated protein abundance of METTL14 was observed in iBAT dissected from *db/db* mice (Fig. 1j, k). METTL14 displayed an inverse relationship with WAT-mediated insulin sensitivity and a positive correlation with BAT-mediated whole-body insulin sensitivity (Fig. 1l–n). Comparable outcomes were evident in the high-fat diet (HFD)-induced obese (DIO) mice compared to the low-fat diet (LFD)-

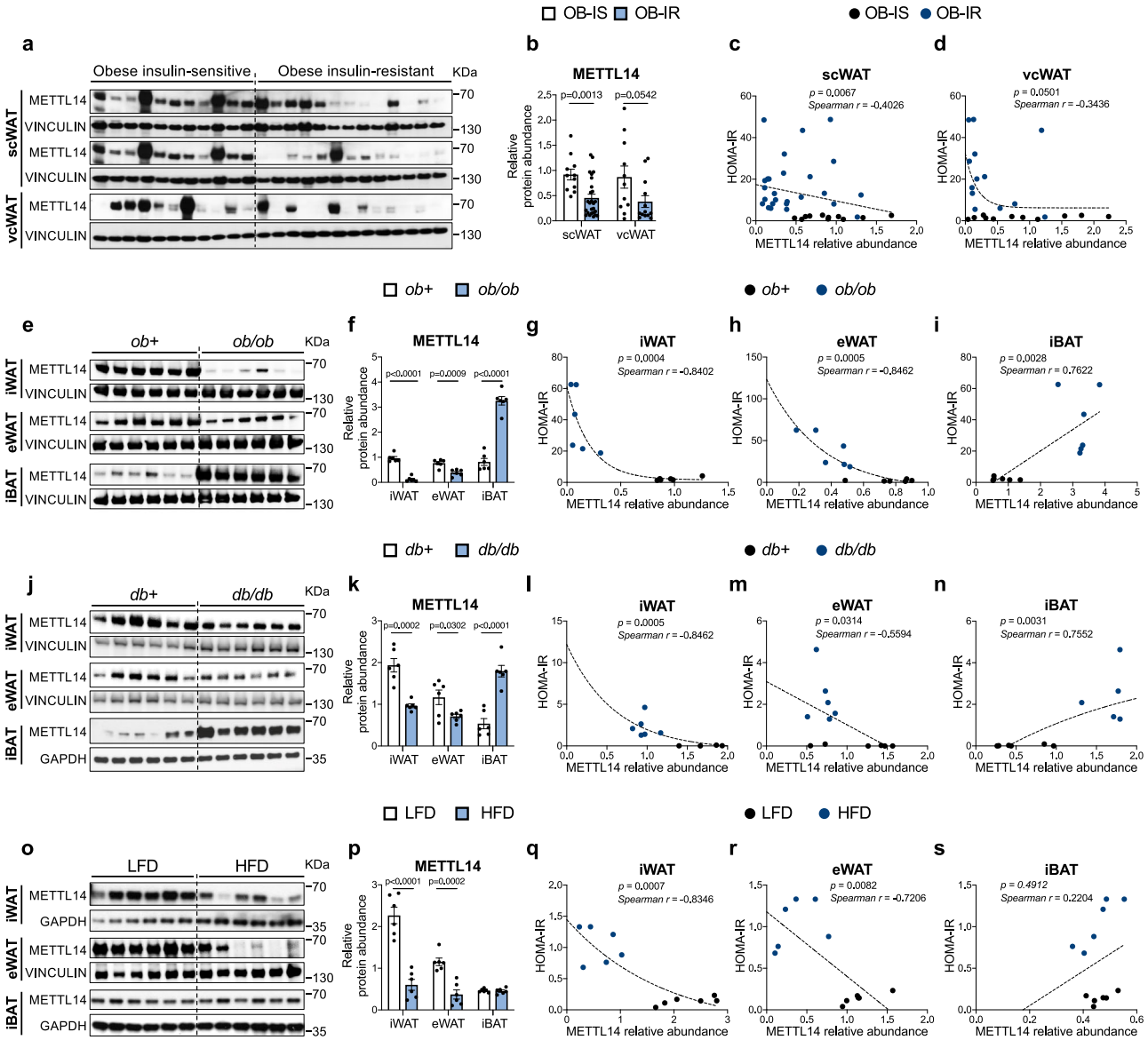

Fig. 1 | METTL14 exhibits differential protein abundance in BAT or WAT from insulin-resistant humans and mice. a, **b** Western blots (**a**) and quantification (**b**) of METTL14 and VINCULIN in subcutaneous and visceral white adipose tissues from individuals with obesity who are insulin-sensitive or insulin-resistant ($n = 11$ for insulin-sensitive individuals with obesity in scWAT and $n = 26$ for insulin-resistant individuals with obesity in scWAT; $n = 11$ for insulin-sensitive individuals with obesity in vcWAT and $n = 13$ for insulin-resistant individuals with obesity in vcWAT). IS, insulin-sensitive; IR, insulin-resistant. scWAT from insulin-sensitive individuals with obesity was loaded in both the upper and lower panels of (**a**) to accommodate the insulin-resistant samples. **c**, **d** Spearman correlation between METTL14 relative abundance in scWAT (**c**) or vcWAT (**d**) and insulin sensitivity, as indicated by HOMA-IR ($n = 11$ for insulin-sensitive individuals with obesity in scWAT and $n = 26$ for insulin-resistant individuals with obesity in scWAT; $n = 11$ for insulin-sensitive individuals with obesity in vcWAT and $n = 13$ for insulin-resistant individuals with obesity in vcWAT). **e**, **f** Western blots (**e**) and quantification (**f**) of METTL14 and VINCULIN in iWAT, eWAT, and iBAT from control (*ob+*) or *ob/ob* mice ($n = 6$/group). iWAT, inguinal white adipose tissue; eWAT, epididymal white adipose tissue; iBAT, interscapular brown adipose tissue. **g**–**i** Spearman correlation between METTL14 relative abundance in iWAT (**g**), eWAT (**h**), or iBAT (**i**) and insulin sensitivity indicated by HOMA-IR ($n = 6$/group). **j**, **k** Western blots (**j**) and quantification (**k**) of METTL14 and VINCULIN or GAPDH in iWAT, eWAT, and iBAT from control (db +) or db/db mice ($n = 6$/group). **l**–**n** Spearman correlation between METTL14 relative abundance in iWAT (**l**), eWAT (**m**), or iBAT (**n**) and insulin sensitivity indicated by HOMA-IR ($n = 6$/group). **o**, **p** Western blots (**o**) and quantification (**p**) of METTL14 and VINCULIN or GAPDH in iWAT, eWAT, and iBAT from LFD- or HFD-fed mice ($n = 6$/group). **q**–**s** Spearman correlation between METTL14 relative abundance in iWAT (**q**), eWAT (**r**), or iBAT (**s**) and insulin sensitivity indicated by HOMA-IR ($n = 6$/group). All samples in each panel are biologically independent. Data are presented as means ± SEM from two independent experiments by two-tailed unpaired t-test (**b**, **f**, **k**, **p**) and one-tailed Spearman correlation (**c**, **d**, **g**–**i**, **l**–**n**, **q**–**s**). See also Supplementary Fig. 1. Source data are provided as a Source Data file.

https://doi.org/10.1038/s41467-024-55694-w

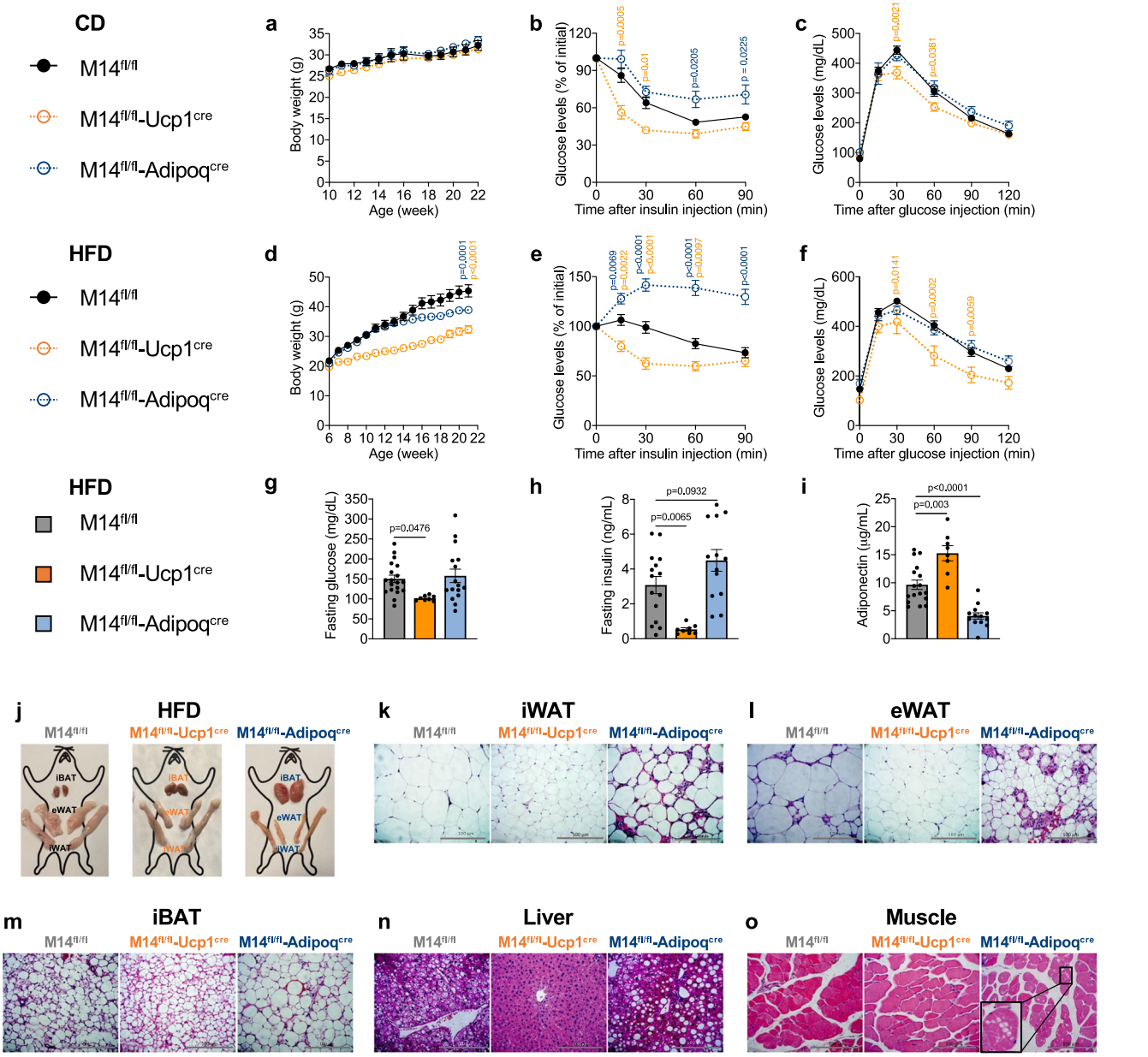

Fig. 2 | Ablation of *Mettl14* in BAT or WAT results in opposite systemic metabolic phenotypes in mice. a Body weight trajectories of CD-fed male mice ($n = 10$/group). **b** Insulin tolerance test of CD-fed male mice ($n = 6$ for $M14^{fl/fl}$ group, $n = 6$ for $M14^{fl/fl}$-$Ucp1^{cre}$ group, and $n = 9$ for $M14^{fl/fl}$-$Adipoq^{cre}$ group). **c** Glucose tolerance test of CD-fed male mice ($n = 14$ for $M14^{fl/fl}$group, $n = 8$ for $M14^{fl/fl}$-$Ucp1^{cre}$ group, and $n = 9$ for $M14^{fl/fl}$-$Adipoq^{cre}$ group). **d** Body weight trajectories of high-fat diet (HFD)-fed male mice ($n = 11$ for $M14^{fl/fl}$group, $n = 8$ for $M14^{fl/fl}$-$Ucp1^{cre}$ group, and $n = 11$ for $M14^{fl/fl}$-$Adipoq^{cre}$ group). **e** Insulin tolerance test of HFD-fed male mice ($n = 11$ for $M14^{fl/fl}$ group, $n = 8$ for $M14^{fl/fl}$-$Ucp1^{cre}$ group, and $n = 11$ for $M14^{fl/fl}$-$Adipoq^{cre}$group). **f** Glucose tolerance test of HFD-fed male mice ($n = 18$ for $M14^{fl/fl}$ group, $n = 8$ for $M14^{fl/fl}$-$Ucp1^{cre}$ group, and $n = 14$ for $M14^{fl/fl}$-$Adipoq^{cre}$ group). **g** Fasting glucose levels in the plasma of $M14^{fl/fl}$, $M14^{fl/fl}$-$Ucp1^{cre}$, and $M14^{fl/fl}$-$Adipoq^{cre}$ male mice ($n = 19$ for $M14^{fl/fl}$ group, $n = 8$ for $M14^{fl/fl}$-$Ucp1^{cre}$ group, and $n = 16$ for $M14^{fl/fl}$-$Adipoq^{cre}$ group). **h** Fasting insulin levels in the plasma of $M14^{fl/fl}$, $M14^{fl/fl}$-$Ucp1^{cre}$, and $M14^{fl/fl}$-$Adipoq^{cre}$ male mice ($n = 15$ for $M14^{fl/fl}$ group, $n = 8$ for $M14^{fl/fl}$-$Ucp1^{cre}$ group, and $n = 13$ for $M14^{fl/fl}$-$Adipoq^{cre}$ group). **i** Fasting adiponectin levels in the plasma of $M14^{fl/fl}$, $M14^{fl/fl}$-$Ucp1^{cre}$, and $M14^{fl/fl}$-$Adipoq^{cre}$ male mice ($n = 17$ for $M14^{fl/fl}$ group, $n = 8$ for $M14^{fl/fl}$-$Ucp1^{cre}$ group, and $n = 13$ for $M14^{fl/fl}$-$Adipoq^{cre}$group). **j** Representative images of the gross appearance of iBAT, iWAT, and eWAT from $M14^{fl/fl}$, $M14^{fl/fl}$-$Ucp1^{cre}$, and $M14^{fl/fl}$-$Adipoq^{cre}$male mice on HFD. **k**–**o** Representative images of H&E stained iWAT (**k**), eWAT (**l**), iBAT (**m**), liver (**n**), and muscle (**o**) from $M14^{fl/fl}$, $M14^{fl/fl}$-$Ucp1^{cre}$, and $M14^{fl/fl}$-$Adipoq^{cre}$male mice on HFD. All samples in each panel are biologically independent. Data are presented as means ± SEM from two independent experiments by Two-way ANOVA (**a**–**f**), and One-way ANOVA (**g**–**i**). Also see Supplementary Figs. 2 and 3. Source data are provided as a Source Data file.

fed group which comprised lean insulin-sensitive mice (Fig. 1o, s). The lack of a significant correlation between METTL14 protein levels in iBAT and whole-body insulin sensitivity could be related, in part, to the short duration of HFD feeding (Fig. 1s). Collectively, these data argue that METTL14 plays a differential role in BAT versus WAT to regulate whole-body metabolism.

Mettl14 deficiency promotes contrasting modulation of BAT- versus WAT-mediated systemic insulin sensitivity in mice

To comprehensively interrogate the divergent roles of METTL14-mediated m^6A modifications in BAT versus WAT and their respective effects on whole-body metabolic processes, we employed a dual approach. Specifically, we generated two distinct lines of knockout

mice by breeding *Mettl14*-floxed ($M14^{fl/fl}$) mice[21], with either a) *Adipoq*-cre mice[22], which facilitated exploration of METTL14's role in the overall functionality of adipose tissue, or b) *Ucp1*-cre mice[23], enabling a focused analysis of BAT-specific *Mettl14* knockout and its repercussions on systemic metabolism (knockouts verified in Supplementary Fig. 2a, b). Both knockout-out lines displayed a typical female and male ratio and normal birth counts. Under CD feeding, both $M14^{fl/fl}$-$Ucp1^{cre}$ and $M14^{fl/fl}$-$Adipoq^{cre}$ male and female mice exhibited similar body weight trajectories compared to the $M14^{fl/fl}$ control group (Fig. 2a for males, Supplementary Fig. 2c for females). Intriguingly, evaluation of glucose homeostasis revealed that $M14^{fl/fl}$-$Ucp1^{cre}$ male and female mice displayed enhanced insulin sensitivity and improved glucose tolerance, while $M14^{fl/fl}$-$Adipoq^{cre}$ mice exhibited diminished insulin sensitivity and similar glucose tolerance as the control $M14^{fl/fl}$ mice (Fig. 2b, c for males, and Supplementary Fig. 2d and e for females).

Upon challenging the mice with an HFD comprising 60% fat for 16 weeks, $M14^{fl/fl}$ control mice exhibited the expected body weight gain and demonstrated compromised insulin sensitivity and glucose intolerance when compared to their low-fat diet (LFD) fed counterparts (data not presented). Both $M14^{fl/fl}$-$Ucp1^{cre}$ and $M14^{fl/fl}$-$Adipoq^{cre}$ male mice displayed significantly lower body weights compared to $M14^{fl/fl}$ mice (Fig. 2d). $M14^{fl/fl}$-$Ucp1^{cre}$ female mice showed consistently lower body weight, while $M14^{fl/fl}$-$Adipoq^{cre}$ females had similar body weight when each group was compared to the control females (Supplementary Fig. 2f). Consistent with our earlier observations[19], $M14^{fl/fl}$-$Ucp1^{cre}$ mice were shielded from HFD-induced systemic insulin resistance and glucose intolerance (Fig. 2e, f for males, Supplementary Fig. 2g, h for females). Conversely, $M14^{fl/fl}$-$Adipoq^{cre}$ mice manifested pronounced insulin resistance, while their glucose tolerance was comparable to the controls (Fig. 2e, f for males, Supplementary Fig. 2g, h for females). Additionally, $M14^{fl/fl}$-$Ucp1^{cre}$ male mice exhibited substantially lower fasting glucose and insulin levels, along with elevated adiponectin levels, whereas $M14^{fl/fl}$-$Adipoq^{cre}$ male mice displayed a different plasma profile characterized by a tendency towards elevated insulin and decreased adiponectin levels (Fig. 2g–i). Notably, both KO mouse models exhibited reduced mass in iWAT and eWAT and increased mass in iBAT compared to controls; the latter was especially pronounced in $M14^{fl/fl}$-$Adipoq^{cre}$ mice (Fig. 2j for males, and Supplementary Fig. 2i for females).

We next examined the characteristics of the different fat mass depots and changes in the liver and skeletal muscle. Hematoxylin and eosin (H&E) staining revealed diminished adipocyte size in both iWAT and eWAT of both knockout mouse models (Fig. 2k, l for males, Supplementary Fig. 2j, k for females). Consistent with prior observations, $M14^{fl/fl}$-$Ucp1^{cre}$ mice were protected from HFD-induced immune cell infiltration in eWAT, hypertrophy of brown adipocytes, and hepatic lipid accumulation (Fig. 2k–n for males, Supplementary Fig. 2j–n for females). In contrast, $M14^{fl/fl}$-$Adipoq^{cre}$ mice displayed heightened immune cell infiltration in both iWAT and eWAT, brown adipocyte hypertrophy, and liver lipid accumulation (Fig. 2k–n for males, Supplementary Fig. 2j–n for females). Strikingly, while both $M14^{fl/fl}$ $M14^{fl/fl}$-$Ucp1^{cre}$ mice displayed normal skeletal muscle morphology, we observed the presence of both inter- and intra-cellular lipid accumulation in the muscle from $M14^{fl/fl}$-$Adipoq^{cre}$ male mice indicating ectopic lipid deposition (Fig. 2o). Thus, manipulation of the expression of *Mettl14* leads to contrasting regulatory roles in terms of insulin sensitivity and systemic metabolism in $Ucp1^{cre}$- and $Adipoq^{cre}$-mediated knockout mouse models.

We next considered that *Mettl14* was depleted in both WAT and BAT in the $M14^{fl/fl}$-$Adipoq^{cre}$ mice (Supplementary Fig. 2a). To specifically investigate the role of *Mettl14* in WAT functionality and overall metabolic control that is independent of iBAT, we surgically removed iBAT from $M14^{fl/fl}$ and $M14^{fl/fl}$-$Adipoq^{cre}$ mice (Supplementary Fig. 3a). Comparing the iBAT-depleted $M14^{fl/fl}$-$Adipoq^{cre}$ mice to iBAT-depleted $M14^{fl/fl}$ mice fed regular CD, revealed that the former persisted in exhibiting insulin resistance (Supplementary Fig. 2b). Of note, iBAT removal exacerbated insulin resistance observed in $M14^{fl/fl}$-$Adipoq^{cre}$ mice as compared to iBAT-depleted $M14^{fl/fl}$ mice (Supplementary Fig. 2b). Additionally, it was noted that in certain $M14^{fl/fl}$-$Adipoq^{cre}$ mice following iBAT removal, there was a conspicuous absence of eWAT and pronounced atrophy in their iWAT, whereas iBAT-depleted $M14^{fl/fl}$ mice exhibited normal gross appearance in their WAT depots (Supplementary Fig. 2c). These observations suggest that while WAT likely plays a dominant role in the phenotype of $M14^{fl/fl}$-$Adipoq^{cre}$ mice, brown adipose tissues, including iBAT, may contribute positively, potentially acting as a metabolic sink for excess triglycerides or FFAs released from WAT. The specific contribution of other BAT depots in addition to iBAT in this context requires further investigation.

Ablation of *Mettl14* in BAT or WAT differentially impacts insulin sensitivity in distinct peripheral metabolic tissues

Next, we examined tissue-autonomous and endocrine effects of *Mettl14* ablation on whole-body insulin sensitivity by injecting mice with insulin via the *vena cava* and assessing changes in insulin signaling proteins (pIRβ/IGF1Rβ and $pAKT_{S473}$) in target metabolic tissues (Fig. 3a). In control mice, HFD decreased insulin-stimulated (1 U/mouse) pIRβ/IGF1Rβ and $pAKT_{S473}$ in iWAT and eWAT compared to LFD (Fig. 3b, c). Insulin resistance induced by the HFD was mitigated in $M14^{fl/fl}$-$Ucp1^{cre}$ mice, evident in both iWAT and eWAT (Fig. 3b, c). However, the insulin response was notably blunted in $M14^{fl/fl}$-$Adipoq^{cre}$ mice in both iWAT and eWAT (Fig. 3b, c).

Furthermore, $M14^{fl/fl}$-$Ucp1^{cre}$ mice on HFD exhibited elevated levels of pIRβ/IGF1Rβ and $pAKT_{S473}$ in iBAT, liver, and skeletal muscle tissues (Fig. 3d–f). Conversely, $M14^{fl/fl}$-$Adipoq^{cre}$ mice displayed reduced insulin signaling in their liver and skeletal muscle, excluding iBAT (Fig. 3d–f). These findings highlight the distinct effects of *Mettl14* ablation in different adipose tissue depots and underscore its role in modulating insulin sensitivity in diverse metabolic tissues.

To investigate the translational significance of our findings in murine models, we capitalized on immortalized human brown and white adipocytes and established stable *METTL14*-knockout cell line colonies in hBAs and hWAs utilizing a single guide RNA targeting METTL14 (sgM14) (Fig. 3g, k, respectively). Notably, the ablation of *METTL14* yielded contrasting effects on insulin sensitivity and glucose uptake capacity in fully differentiated hBAs (Fig. 3h–j) versus hWAs (Fig. 3l–n). These observations support the notion that METTL14 regulates insulin sensitivity in a context- and cell-type-dependent manner.

Mettl14 deficiency in BAT or WAT differentially impacts food intake and energy expenditure in mice

Next, we investigated whether METTL14 differentially modulates BAT- or WAT-mediated whole-body energy balance. *Mettl14* deficiency utilizing $Ucp1^{cre}$ exhibited an enhanced cold tolerance (Fig. 4a) without significant alterations in food intake (Fig. 4b), oxygen consumption (Fig. 4c), or energy expenditure (Fig. 4d). Conversely, $M14^{KO}$ driven by $Adipoq^{cre}$ resulted in a significant reduction in thermogenic capacity (Fig. 4a), food intake (Fig. 4b), oxygen consumption (Fig. 4e), and energy expenditure (Fig. 4f). Similarly, at the cellular level, *METTL14* deficiency showed no significant impact on the basal (Fig. 4g–j) or β3-adrenergic agonist-stimulated (Figs. 4k–n) mitochondrial and glycolytic functions of hBAs, while, the absence of *METTL14* in hWAs negatively regulated these functions (Fig. 4o–r). Previous studies have reported that METTL3 positively regulates thermogenesis in both BAT-specific ($Ucp1^{cre}$ driven-knockout) and beige-specific ($Adipoq^{cre}$-mediated knockout) mouse models[15,17]. Our findings highlight the intricate and diverse roles of the m^6A writer protein, METTL14, in the regulation of thermogenesis and metabolic control in adipose tissues, and unlike METTL3, METTL14 can regulate the thermogenesis of adipose tissues in a cell-specific manner.

https://doi.org/10.1038/s41467-024-55694-w

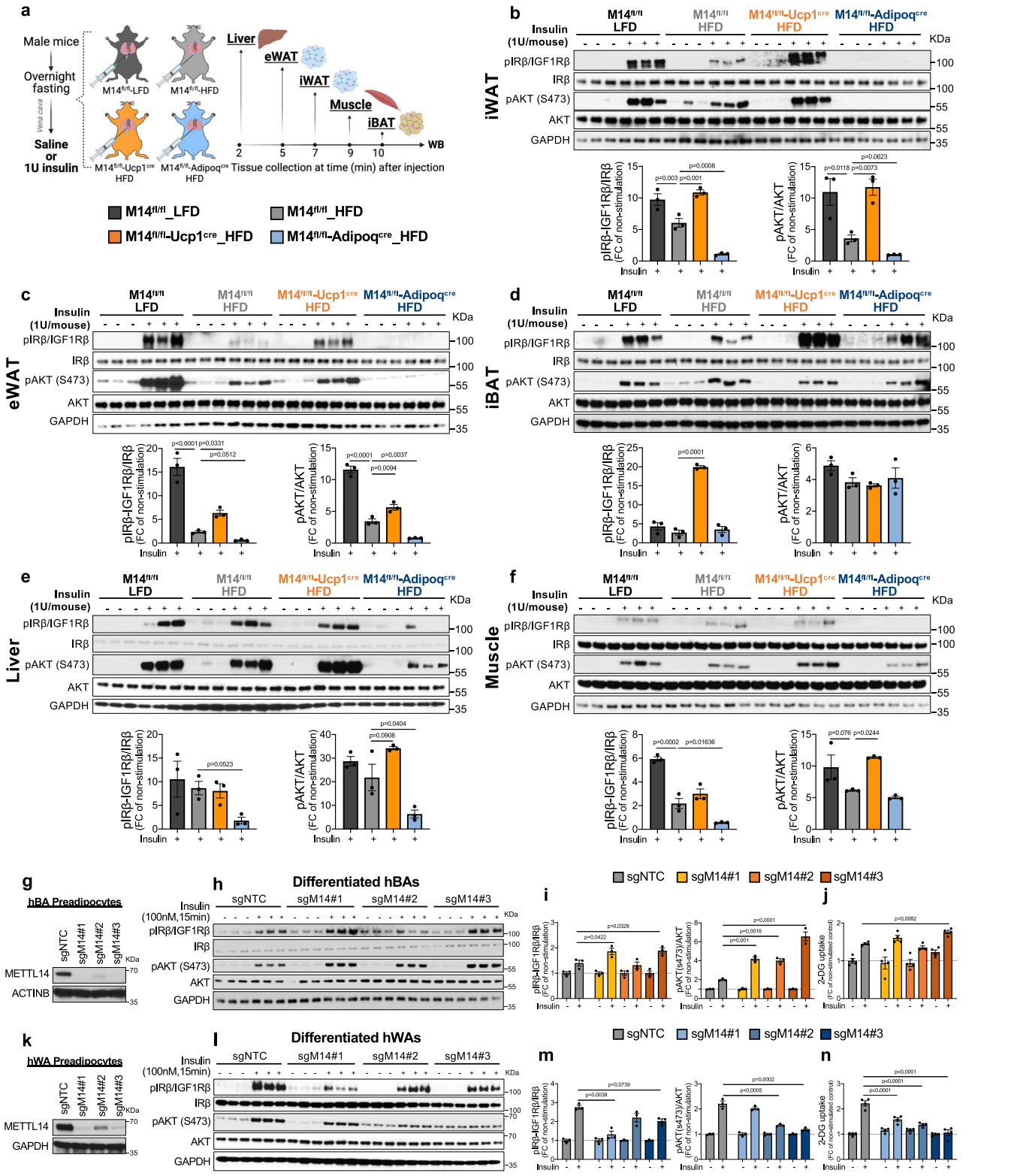

Mettl14 Deficiency Differentially Impacts m^{6}A Methylome and Transcriptome in Mouse iBAT and iWAT

The distinct roles of METTL14 in BAT- versus WAT-mediated whole-body metabolism prompted the hypothesis that METTL14 differentially modulates the transcriptional profiles of BAT and WAT by selectively methylating specific target transcripts. To test this hypothesis, we conducted m^{6}A-MeRIP-seq and RNA-seq analyses on iBAT from M14$^{fl/fl}$ and M14$^{fl/fl}$-Ucp1^{cre} mice, as well as iWAT from M14$^{fl/fl}$ and M14$^{fl/fl}$-Adipoq^{cre} mice.

First, a comparison of the m^{6}A methylome between M14$^{fl/fl}$-Ucp1^{cre}-iBAT versus M14$^{fl/fl}$-iBAT, and between M14$^{fl/fl}$-Adipoq^{cre}-iWAT versus M14$^{fl/fl}$-iWAT (comparison approach shown in Fig. 5a) revealed 2465 and 2838 m^{6}A-hypomethylated genes (Fig. 5b), as well as 4854 and 8007 hypermethylated genes by *Mettl14* deficiency in iBAT and iWAT respectively (Fig. 5c). *Mettl14* deficiency resulted in 1375 and 1748 m^{6}A-hypermethylated genes (Fig. 5b), as well as 2010 and 5163 m^{6}A-hypermethylated genes exclusively in iBAT and iWAT, respectively (Fig. 5b). Next, the intersection of the differentially m^{6}A-modified

Fig. 3 | Ablation of *Mettl14* in BAT or WAT differentially impacts insulin sensitivity of peripheral metabolic tissues. a Diagram illustrating the timeline for collecting metabolic tissues following saline/insulin injection into the *vena cava* of $M14^{fl/fl}$, $M14^{fl/fl}$-$Ucp1^{cre}$, and $M14^{fl/fl}$-$Adipoq^{cre}$ male mice fed either a low-fat diet (LFD) or a high-fat diet (HFD) ($n = 6$/group) as indicated (Created with BioRender.com). **b**–**f** Western blot analysis and quantification of insulin-stimulated phosphorylation of IRβ/IGF1Rβ and AKT_{S473} in iWAT (**b**), eWAT (**c**), iBAT (**d**), liver (**e**), and muscle (**f**) after injection of 1U insulin into the *vena cava* ($n = 6$/groups). **g** Western blot analysis of METTL14 protein abundance in sgNTC-, sgM14#1-, sgM14#2-, sgM14#3-hBA preadipocytes. **h**, **i** Western blot analysis (**h**) and quantification (**i**) of insulin-stimulated phosphorylation of IRβ/IGF1Rβ and AKT_{S473} in differentiated sgNTC-, sgM14#1-, sgM14#2-, sgM14#3-hBA cells ($n = 6$/group). **j** Glucose uptake of differentiated sgNTC-, sgM14#1-, sgM14#2-, sgM14#3-hBA cells treated with or without insulin stimulation ($n = 4$/group). **k** Western blot analysis of METTL14 protein abundance in sgNTC-, sgM14#1-, sgM14#2-, sgM14#3-hWA preadipocytes. **l**, **m** Western blot analysis (**l**) and quantification (**m**) of insulin-stimulated phosphorylation of IRβ/IGF1Rβ and AKT_{S473} in differentiated sgNTC-, sgM14#1-, sgM14#2-, sgM14#3-hWA cells ($n = 6$/group). **n** Glucose uptake of differentiated sgNTC-, sgM14#1-, sgM14#2-, sgM14#3-hWA cells treated with or without insulin stimulation ($n = 4$/group). All samples in each panel are biologically independent. Data are presented as means ± SEM from two or three independent experiments by Two-way ANOVA (**b**–**f**, **i**, **j**, **m**, **n**). Also see Supplementary Fig. 4. Source data are provided as a Source Data file.

genes in $M14^{fl/fl}$-$Ucp1^{cre}$-iBAT and $M14^{fl/fl}$-$Adipoq^{cre}$-iWAT revealed 1090 (25.9%) and 2844 (28.4%) commonly hypomethylated and hypermethylated genes compared to $M14^{fl/fl}$ mice, respectively (Fig. 5b, c).

Similar comparisons were performed between the differentially expressed genes in $M14^{fl/fl}$-$Ucp1^{cre}$-iBAT and $M14^{fl/fl}$-$Adipoq^{cre}$-iWAT (Fig. 5a). Only 106 genes (2.8% of total upregulated genes) exhibited overlap between $M14^{fl/fl}$-$Ucp1^{cre}$ iBAT and $M14^{fl/fl}$-$Adipoq^{cre}$ iWAT (Fig. 5d), and 91 (1.8%) genes were commonly downregulated (Fig. 5e). Gene set enrichment analysis revealed significant divergence in the transcriptional programs of METTL14 between BAT and WAT (Fig. 5f–i). Upregulated genes of $M14^{fl/fl}$-$Ucp1^{cre}$ iBAT were enriched in pathways related to lipid metabolism, prostaglandin synthesis, and phospholipid biosynthetic processes (Fig. 5f), while downregulated genes were associated with insulin resistance, white fat cell differentiation, and apoptosis pathways (Fig. 5g). In contrast, $M14^{fl/fl}$-$Adipoq^{cre}$ iWAT showed upregulation of pathways involving immune response, TNFα signaling, and apoptosis (Fig. 5h), with downregulated genes enriched in lipid metabolism, lipolysis, insulin signaling, and phospholipid metabolism pathways (Fig. 5i).

Considering that METTL14 is responsible for installing m^6A, the depletion of METTL14 is expected to result in the hypomethylation of its target transcripts. Moreover, it is established that reduced m^6A methylation correlates with enhanced mRNA stability, as it protects the target transcripts from degradation[19,21,24]. To clarify if these transcriptomic changes were governed by METTL14-mediated m^6A modification, we intersected m^6A-hypomethylated and differentially upregulated genes. These analyses confirmed that lipid and phospholipid-related pathways were m^6A-dependently upregulated in $M14^{fl/fl}$-$Ucp1^{cre}$ iBAT (Fig. 5j, k), while apoptosis and TNFα signaling pathways were upregulated in an m^6A-dependent manner in $M14^{fl/fl}$-$Adipoq^{cre}$ iWAT (Fig. 5l, m).

METTL14 selectively methylates key target transcripts in hBAs versus hWAs

Given the marked cellular heterogeneity of BAT and WAT tissues[25,26], we harnessed hBA and hWA models to delve into the cellular-level transcriptional mechanism(s) influenced by METTL14. Using the same comparison strategy described above, the intersection of m^6A hypomethylated genes in sgM14-hBAs and sgM14-hWA cells revealed only 160 (6.3%) commonly hypomethylated and 912 (14.2%) hypermethylated genes, along with 559 (11.8%) commonly upregulated and 554 (11.9%) commonly downregulated genes (Fig. 6a–d).

In hBA cells, enrichment analyses of the DGE (differentially gene expression) pointed to elevated lipid metabolism and phospholipid processes among upregulated pathways, and apoptosis and TNFα signaling among the prominent downregulated pathways due to *METTL14* deficiency (Fig. 6e, f). Conversely, in hWA cells, *METTL14* deficiency predominantly led to m^6A-dependent upregulation of TNFα and apoptosis pathways (Fig. 6g, i, j), while resulting in the downregulation of pathways regulated by EGFR1, focal adhension-PK3K-AKT-mTOR, and insulin signaling (Fig. 6h).

Importantly, while the stable knockout cell line enables the conduct of several phenotypical and mechanistic studies, the ablation of *METTL14* in preadipocytes may also influence the differentiation process of both hWAs and hBAs. To address this potential confounding factor in adipocyte differentiation, we performed a transient knockdown of *METTL14* using siRNA in fully differentiated adipocytes, (Fig. 6k). Consistently, *METTL14* deficiency in mature hWA cells accentuated the significance of TNFα and cell death signaling pathways (Fig. 6l, m). These findings emphasize the ability of METTL14 to exhibit divergent roles in shaping the transcriptional profiles of mature brown adipocytes to promote a favorable metabolic phenotype. Conversely, in the $M14^{fl/fl}$-$Adipoq^{cre}$ model, *METTL14* deficiency distinctly upregulated genes linked to TNFα and apoptosis in mature white adipocytes, contributing to adipose tissue apoptosis and insulin resistance. Thus, at both tissue and cellular levels, *METTL14* deficiency leads to an upregulation of genes encoding prostaglandin synthases in BAT, and key genes related to TNFα signaling and apoptosis in WAT.

As mentioned above, *METTL14* deficiency is expected to induce hypomethylation in its target transcripts. Next, we conducted further analysis to explore the m^6A-hypomethylated and upregulated genes, which are considered METTL14-targeted transcripts, within the most enriched pathways of sgM14-hBAs cells and sgM14-hWA cells. Within hBA cells, METTL14 specifically destabilizes transcripts associated with prostaglandin synthesis[19]. In this study, we identified five transcripts—necrosis factor-related apoptosis-inducing ligand (*TRAIL*), TNF receptor superfamily member 1A (*TNFR1*), receptor-interacting serine/threonine kinase 1 (*RIP*), caspase 7 (*CASP7*), and DNA fragmentation factor subunit alpha (*DFFA*), as direct targets of METTL14 in hWA cells (Fig. 6n). Interestingly, while *METTL14* deficiency led to the upregulation of several genes within the TNFα and apoptosis pathways in hWA cells, most of these genes exhibited downregulation in sgM14-hBA cells (Fig. 6o). Notably, transcripts previously identified as METTL14 targets in hBA, including *PTGES2*, *CRB1*, and *PGC1A*, were downregulated in sgM14-hWA compared to sgNTC-hWA cells (Fig. 6p). These findings provide strong evidence that METTL14 regulates distinct transcriptional processes in BAT versus WAT, as summarized in Fig. 6q.

METTL14 deficiency promotes apoptosis in mouse and human white adipocytes

We next sought to validate our sequencing outcome and investigate the molecular mechanism(s) underlying the METTL14-mediated m^6A decoration of target transcripts in brown versus white adipocytes/adipose tissues.

METTL14 deficiency promotes prostaglandin synthesis in brown adipocytes, as reported in our previous study[19]. To validate our sequencing outcome from mouse and human white adipocytes, which indicate increased apoptosis (Figs. 5 and 6), we conducted Terminal deoxynucleotidyl Transferase dUTP Nick End Labeling (TUNEL) assays on the iWAT and eWAT isolated from $M14^{fl/fl}$-$Adipoq^{cre}$ mice. Our data confirmed a higher percentage of apoptotic cells in both depots (Fig. 7a–c). Notably, apoptosis was primarily observed in PERILIPIN-

https://doi.org/10.1038/s41467-024-55694-w

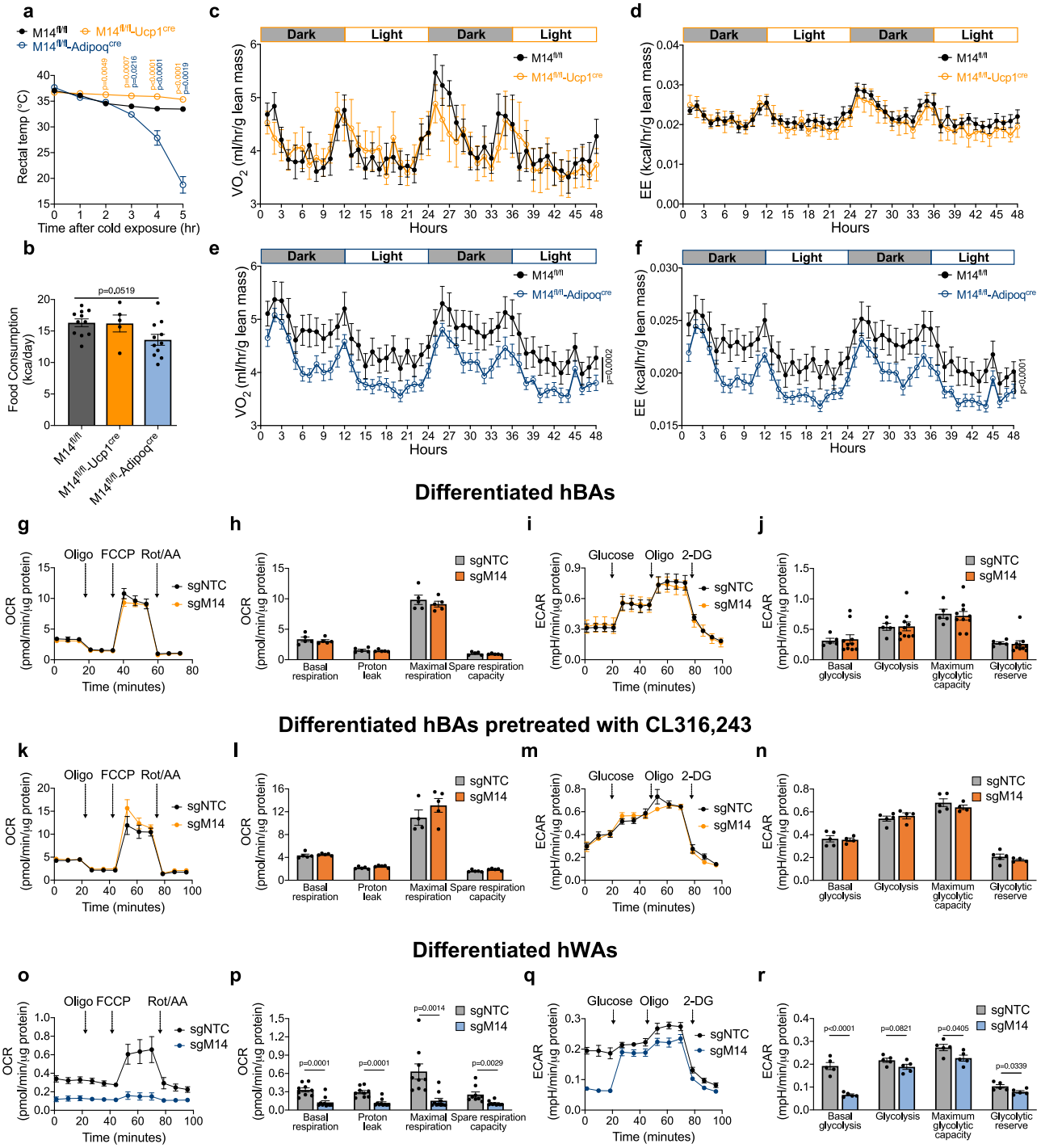

Fig. 4 | *Mettl14* Deficiency Differentially Regulates Thermogenic Capacity of BAT and WAT. a Core body temperature of M14$^{fl/fl}$, M14$^{fl/fl}$-Ucp1^{cre}, and M14$^{fl/fl}$-Adipoq^{cre} mice after acute cold exposure ($n = 15$ for M14$^{fl/fl}$ group, $n = 8$ for M14$^{fl/fl}$-Ucp1^{cre} group, and $n = 6$ for M14$^{fl/fl}$-Adipoq^{cre} group). **b** Daily food consumption measured by indirect calorimetry ($n = 11$ for M14$^{fl/fl}$ group, $n = 5$ for M14$^{fl/fl}$-Ucp1^{cre} group, and $n = 11$ for M14$^{fl/fl}$-Adipoq^{cre} group). **c**, **d** Oxygen consumption (**c**) and energy expenditure (**d**) of M14$^{fl/fl}$-Ucp1^{cre} mice versus M14$^{fl/fl}$ mice ($n = 6$ for M14$^{fl/fl}$ group, $n = 5$ for M14$^{fl/fl}$-Ucp1^{cre} group). **e**, **f** Oxygen consumption (**e**) and energy expenditure (**f**) of M14$^{fl/fl}$-Adipoq^{cre} mice versus M14$^{fl/fl}$ mice ($n = 11$/group). **g**–**j** Seahorse analysis of cellular oxygen consumption rate (OCR) (**g**, **h**, $n = 5$/group) and extracellular acidification rate (ECAR) (**i**, **j**, $n = 5$ for sgNTC, and $n = 10$ for sgM14) in differentiated sgNTC- and sgM14-hBA cells. **k**–**n** Seahorse analysis of cellular oxygen consumption rate (OCR) (**k**, **l**, $n = 5$/group) and extracellular acidification rate (ECAR) (**m**, **n**, $n = 4$ for sgNTC, and $n = 5$ for sgM14) in differentiated sgNTC- and sgM14-hBA cells stimulated with 10 μM CL-316,243 for 5 h before seahorse assay. **o**–**r** Seahorse analysis of cellular oxygen consumption rate (OCR) (**o**, **p**, $n = 9$ for sgNTC, and $n = 10$ for sgM14) and extracellular acidification rate (ECAR) (**q**, **r**, $n = 5$/group) in differentiated sgNTC- and sgM14-hWA cells (Data are representative of 2 independent experiments). All samples in each panel are biologically independent. Data are presented as means ± SEM from two or three independent experiments by Two-way ANOVA with Dunnett's multiple comparisons test (**a**, **b**), Two-way ANOVA (**c**–**g**, **i**, **k**, **m**, **o**, **q**), and Two-tailed unpaired t-tests (**h**, **j**, **l**, **n**, **p**, **r**). Source data are provided as a Source Data file.

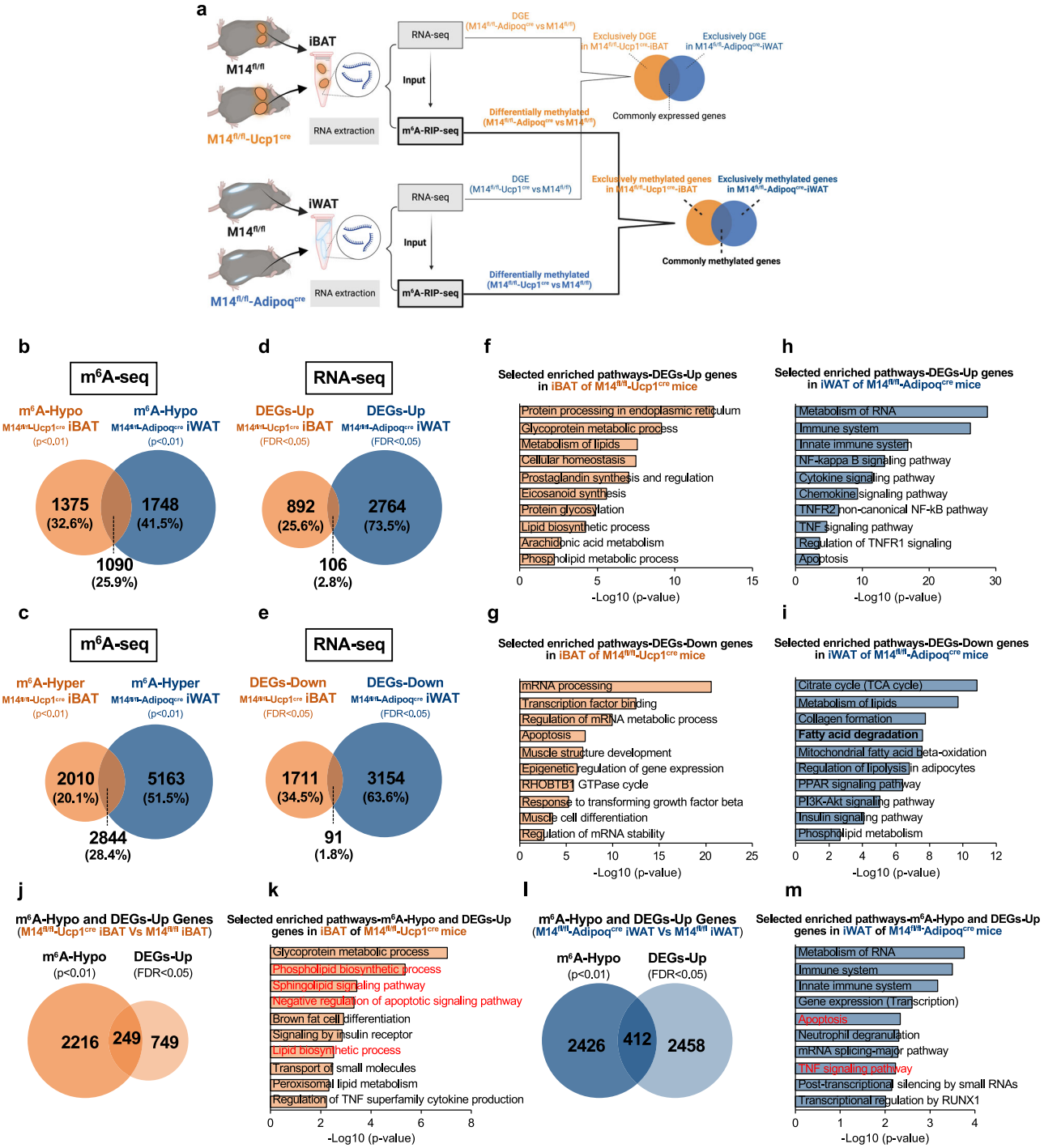

positive cells (Fig. 7a), suggesting adipocyte-specific apoptosis induced by *METTL14* deficiency.

In mouse iBAT and differentiated hBAs, METTL14-mediated m^{6}A installation promotes the decay of transcripts related to prostaglandin synthesis in a YTHDF2/3-dependent manner[19]. In iWAT, *Mettl14* deficiency leads to upregulation of *Trail, Dr5, Tnfa, Tnfr1, Casp3, Casp7*, and *Dffa* at the mRNA level (Fig. 7d), and increased protein abundance of TRAIL and TNFA (Fig. 7e, f).

Considering the ectopic fat deposition in iBAT, liver, and muscle (Fig. 1m–o), we wondered whether apoptosis of white adipocytes increases circulating free fatty acids (FFAs) and/or triglyceride (TG) levels, leading to iBAT hypertrophy, hepatic steatosis and/or muscle lipid accumulation. Since *Mettl14* deficiency downregulated genes associated with fatty acid degradation (also referred to as lipolysis) and regulation of lipolysis in adipocyte pathways (Fig. 5h), it is plausible that lipolysis-induced FFA production does not contribute to ectopic lipid accumulation. Indeed, FFA levels (Fig. 7g) were lower while TG levels (Fig. 7h) were elevated in the serum of M14$^{fl/fl}$-Adipoq^{cre} mice compared to control mice. Moreover, the TG level was higher in the liver of HFD-fed and CD-fed iBAT-deficient M14$^{fl/fl}$-Adipoq^{cre} mice; as well as higher in the liver of HFD-fed Adipoq^{cre} mice (Fig. 7i).

Consistent results were obtained at the cellular level, as indicated by the upregulated gene expression and protein abundance of apoptotic markers (Fig. 7j, k, respectively), decreased levels of FFAs, and heightened TGs in the conditioned media of differentiated sgM14-hWA cells (Fig. 7l). Of note, the levels of both cleaved caspase 3 (cCASP3) and caspase 7 (cCASP7) were significantly increased in the sgM14-hWA cell line (Fig. 7k), providing further support for adipocyte-specific

Fig. 5 | *Mettl14* Deficiency Results in Different m^{6}A Methylome and Transcriptome of Mouse iBAT and iWAT. a Schematic diagram of comparison approach for analyzing RNA-seq and m^{6}A-seq data derived from iWAT in M14$^{fl/fl}$ and M14$^{fl/fl}$-Adipoq^{cre} mice, and from iBAT in M14 $^{fl/fl}$ and M14$^{fl/fl}$-Ucp1^{cre} mice (Created with BioRender.com). **b** Venn diagram representation of the exclusively m^{6}A-hypomethylated genes in M14$^{fl/fl}$-Ucp1^{cre}-iBAT versus M14$^{fl/fl}$-iBAT, commonly m^{6}A-hypomethylated genes, and exclusively m^{6}A-hypomethylated genes in M14$^{fl/fl}$-Adipoq^{cre}-iWAT versus M14$^{fl/fl}$-iWAT, statistical analyses were performed using the Benjamin-Hochberg procedure and genes were filtered for $p < 0.01$. **c** Venn diagram representation of the exclusively m^{6}A-hypermethylated genes in M14$^{fl/fl}$-Ucp1^{cre}-iBAT versus M14$^{fl/fl}$-iBAT, commonly m^{6}A-hypermethylated genes, and exclusively m^{6}A-hypermethylated genes in M14$^{fl/fl}$-Adipoq^{cre}-iWAT versus M14$^{fl/fl}$-iWAT, statistical analyses were performed using the Benjamin-Hochberg procedure and genes were filtered for $p < 0.01$. **d** Venn diagram representation of the exclusively upregulated genes in M14$^{fl/fl}$-Ucp1^{cre}-iBAT versus M14$^{fl/fl}$-iBAT, commonly upregulated genes, and exclusively upregulated genes in M14$^{fl/fl}$-Adipoq^{cre}-iWAT versus M14$^{fl/fl}$-iWAT, statistical analyses were performed using the Benjamin-Hochberg procedure and genes were filtered for FDR < 0.05. **e** Venn diagram representation of the exclusively downregulated genes in M14$^{fl/fl}$-Ucp1^{cre}-iBAT versus M14$^{fl/fl}$-iBAT, commonly downregulated genes, and exclusively downregulated genes in M14$^{fl/fl}$-Adipoq^{cre}-iWAT versus M14$^{fl/fl}$-iWAT, statistical analyses were performed using the Benjamin-Hochberg procedure and genes were filtered for FDR < 0.05. **f**, **g** Enriched pathways of the upregulated (**f**) or downregulated **g** genes in M14$^{fl/fl}$-Ucp1^{cre}-iBAT versus M14$^{fl/fl}$-iBAT. **h**, **i** Enriched pathways of the upregulated (**h**) or downregulated (**i**) genes in M14$^{fl/fl}$-Adipoq^{cre}-iWAT versus M14$^{fl/fl}$-iWAT. **j** Venn diagram representation of the m^{6}A-hypomethylated ($p < 0.01$) and upregulated genes (FDR < 0.05) in M14$^{fl/fl}$-Ucp1^{cre}-iBAT versus M14$^{fl/fl}$-iBAT. **k** Top 10 enriched pathways of the m^{6}A-hypomethylated and differentially upregulated genes in M14$^{fl/fl}$-Ucp1^{cre}-iBAT versus M14$^{fl/fl}$-iBAT. **l** Venn diagram representation of the m^{6}A-hypomethylated ($p < 0.01$) and upregulated genes (FDR < 0.05) in M14$^{fl/fl}$-Adipoq^{cre}-iWAT versus M14$^{fl/fl}$-iWAT. **m** Top 10 enriched pathways of the m^{6}A-hypomethylated and differentially upregulated genes in M14$^{fl/fl}$-Adipoq^{cre}-iWAT versus M14$^{fl/fl}$-iWAT. *p*-values of pathway enrichment analysis were calculated according to the hypergeometric test based on the number of physical entities present in both the predefined set and user-specified list of physical entities (**f**–**i**, **m**). Source data are provided as a Source Data file.

apoptosis. These data collectively indicate that M14^{KO}-WAT apoptosis-induced lipid spillover contributes to the observed ectopic lipid accumulation and consequent peripheral insulin resistance (Fig. 7m).

METTL14-Mediated m^{6}A accelerates the decay of apoptosis-related transcripts in A YTHDF2/3-dependent manner in white adipocytes

Next, we conducted mechanistic studies using differentiated hWA cells. First, we examined the effects of *METTL14* deficiency on the stability of m^{6}A-targeted mRNAs (identified in Fig. 6n) following treatment with transcription inhibitor actinomycin D (ActD). *METTL14* deficiency suppressed the degradation of *TRAIL* and *TNFR1* mRNAs without significantly affecting the stability of ACTINB mRNA (Fig. 8a). These findings suggest that METTL14-mediated m^{6}A modification orchestrates hWA apoptosis by regulating the stability of key apoptotic transcripts.

To further confirm this hypothesis, we performed independent siRNA-mediated knockdown of the m^{6}A reader proteins YTHDF1, YTHDF2, or YTHDF3 (Fig. 7i), which are known to regulate mRNA decay[24,27], and examined the expression and stability of *TRAIL* and *TNFR1* mRNAs after ActD treatment in wild type hWA cells. Knockdown of YTHDF1, YTHDF2, or YTHDF3 (Fig. 8b) followed by ActD treatment significantly increased the stability of *TRAIL* and *TNFR1* (Fig. 8c). These data collectively confirmed that METTL14-mediated m^{6}A installation negatively regulates the stability of *TRAIL* and *TNFR1* mRNAs in white adipocytes.

Next, to substantiate the implication that METTL14 is linked to the modulation of mRNA stability of apoptosis-associated genes, we explored this possibility with a gain-of-function model by overexpressing *METTL14* in hWA cells (Fig. 8d, e). Additionally, to investigate whether METTL14 regulates key target mRNA stability in an m^{6}A-dependent manner, we established a hWA cell line harboring the METTL14 R298 mutation (Fig. 8d, e). As expected, overexpression of *METTL14* increased global m^{6}A levels, whereas mutated METTL14 had no impact (Fig. 8f). Importantly, while METTL14 upregulation led to decreased stability of *TRAIL* and *TNFR1* through m^{6}A hypermethylation, their stability was not affected by mutated METTL14 in hWA cells (Fig. 8g). These findings support that METTL14 directly regulates *TRAIL* and *TNFR1* in an m^{6}A-dependent manner.

Finally, to validate our identification of TRAIL and TNFR1 as drivers of systemic insulin resistance in M14$^{fl/fl}$-Adipoq^{cre} mice, we used AAV8 vectors to genetically knock down *Trail* or *Tnfr1* specifically in iWAT by injecting AAV8-scramble, AAV8-shTrail, or AAV8-shTnfr1 (Fig. 8h). Knockdown efficiency was confirmed by reduced TRAIL or TNFR1 protein levels in iWAT (Fig. 8i, j). Notably, knockdown of each gene significantly decreased serum triglyceride (TG) levels in M14$^{fl/fl}$-Adipoq^{cre} mice (Fig. 8k), affirming that TRAIL and TNFR1 triggered adipocyte apoptosis and subsequent lipid spillover. Additionally, depletion of either *Trail* or *Tnfr1* partially reversed insulin resistance in M14$^{fl/fl}$-Adipoq^{cre} mice at both the systemic and tissue levels (Fig. 8l–n, respectively).

Discussion

An accumulating body of evidence points to the importance of m^{6}A mRNA modifications in orchestrating pathways that underlie intricate mechanisms that contribute to metabolic disorders[28]. However, the current gap in our understanding pertains to the cell-type-specific regulation by m^{6}A within various biological domains, including metabolism. Here, we provide one example of the divergent roles of METTL14-mediated m^{6}A modifications in orchestrating the metabolic functions of brown versus white adipocytes. By integrating m^{6}A-seq and RNA-seq obtained from both mouse BAT/WAT and human brown/white adipocytes, we unveil cell-type specific m^{6}A methylomes and transcriptomes. Our study identifies specific transcripts through which METTL14 exerts dual regulatory roles: on one hand, negatively modulating the secretory functions of BAT while on the other simultaneously enhancing the lipid sequestration capabilities of WAT. This multifaceted role of METTL14 in shaping adipocyte-mediated metabolism adds a new layer of nuance to the field of metabolic regulation.

Notably, while the M14$^{fl/fl}$-Ucp1^{cre} model was featured in our recent report[19], the current study includes newly generated data from a different cohort of animals in this model, which is essential as it provides a critical BAT-specific knockout for comparison with the overall-adipose knockout (M14$^{fl/fl}$-Adipoq^{cre}) model. This approach allows us to differentiate BAT-specific effects from those in total adipose tissue. Furthermore, the consistency of findings in different cohorts of animals demonstrates the reproducibility and robustness of our experimental approach, further validating the significance of our results.

A study recently reported by Kang and colleagues[29] also used the M14$^{fl/fl}$-Adipoq^{cre} mouse model to create an adipose-specific *Mettl14*-knockout. While our study, as well as the study by Kang et al., observed decreased body weight, impaired cold tolerance, decreased WAT mass, and increased BAT mass, several obvious differences stand out when comparing the two reports: First, while the major findings in the Kang et al. study exclusively rely on the Mettl14$^{fl/fl}$-Adipoq^{cre} model, it was surprising that no information regarding the origin of Mettl14$^{fl/fl}$ mice and the KO targeting strategy (e.g., which exons are floxed) was provided, which limits the comparison between our KO model and theirs. On the other hand, we and several other groups have characterized our Mettl14$^{fl/fl}$ mice[21,30]. Second, in their study, Kang et al surprisingly do not use m^{6}A-seq but bulk RNA-seq to determine targets that contribute to the phenotype. In contrast, we used m^{6}A-MeRIP- and

https://doi.org/10.1038/s41467-024-55694-w

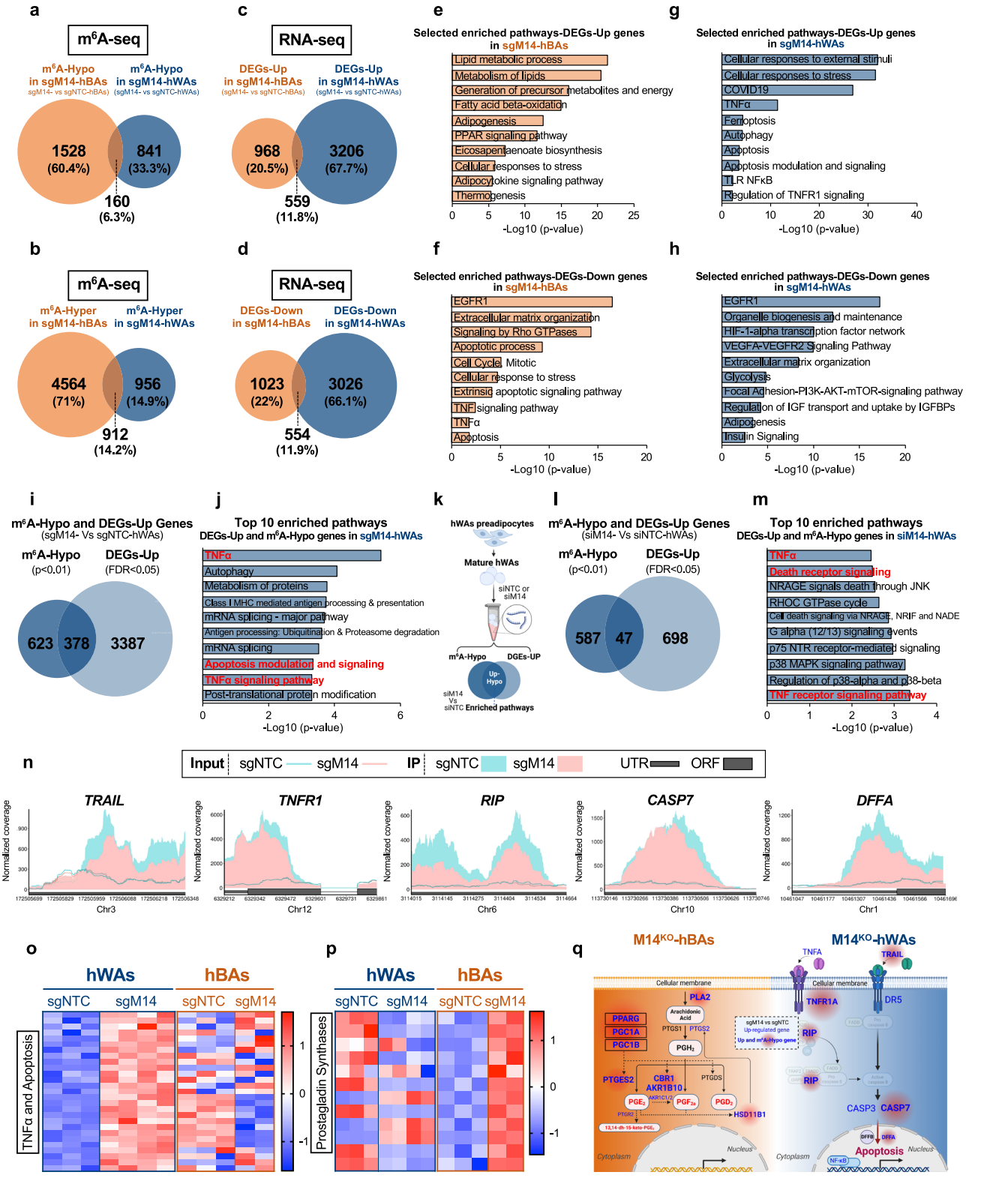

RNA-seq as drivers to determine the mechanism(s) that underlie the phenotype. Considering METTL14's non-m^{6}A-dependent effects, it is likely the approach by Kang et al. introduced bias in the identification of m^{6}A-targeted genes. Third, in their study, Kang et al. attribute decreased body weight, enhanced insulin sensitivity, and improved glucose tolerance to heightened cell-autonomous lipolysis resulting from *Mettl14* deficiency. This conclusion is inconsistent with the large body of literature demonstrating that excessive lipolysis, particularly in white adipocytes, contributes to adipose tissue- and systemic "insulin resistance"[31–34]. The exacerbated insulin resistance is secondary to the influx of elevated circulating FFAs into non-adipose tissues and the release of proinflammatory cytokines[31], both of which interfere with insulin signaling. Kang et al. noted increased circulating FFAs, improved hepatic insulin sensitivity and steatosis in their model, while reduced *Tnfα* and *Il6* gene expression in M14^{KO} adipose tissue, confounding the overall interpretation of the phenotype[29]. Finally, insulin

Fig. 6 | METTL14 Selectively Methylates Key Target Transcripts in hBA versus hWA cells. a Venn diagram representation of the exclusively m^{6}A-hypomethylated genes in sgM14-hBA versus sgNTC-hBA cells, commonly m^{6}A-hypomethylated genes, and exclusively m^{6}A-hypomethylated genes in sgM14-hWA versus sgNTC-hWA cells, statistical analyses were performed using the Benjamin-Hochberg procedure and genes were filtered for $p < 0.01$. **b** Venn diagram representation of the exclusively m^{6}A-hypermethylated genes in sgM14-hBA versus sgNTC-hBA cells, commonly m^{6}A-hypermethylated genes, and exclusively m^{6}A-hypermethylated genes in sgM14-hWA versus sgNTC-hWA cells, statistical analyses were performed using the Benjamin-Hochberg procedure and genes were filtered for $p < 0.01$. **c** Venn diagram representation of the exclusively upregulated genes in sgM14-hBA versus sgNTC-hBA cells, commonly upregulated genes, and exclusively upregulated genes in sgM14-hWA versus sgNTC-hWA cells, statistical analyses were performed using the Benjamin-Hochberg procedure and genes were filtered for FDR < 0.01. **d** Venn diagram representation of the exclusively downregulated genes in sgM14-hBA versus sgNTC-hBA cells, commonly downregulated genes, and exclusively downregulated genes in sgM14-hWA versus sgNTC-hWA cells, statistical analyses were performed using the Benjamin-Hochberg procedure and genes were filtered for FDR < 0.01. **e**, **f** Enriched pathways of the upregulated (**e**) or downregulated (**f**) genes in sgM14-hBA versus sgNTC-hBA cells. **g**, **h** Enriched pathways of the upregulated (**g**) or downregulated (**h**) genes in sgM14-hWAs versus sgNTC-hWA cells. **i** Venn diagram representation of the m^{6}A-hypomethylated and upregulated genes in sgM14-hWA versus sgNTC-hWA cells, statistical analyses were performed using the Benjamin-Hochberg procedure and genes were filtered for $p < 0.01$, and FDR < 0.05, respectively. **j** Top 10 enriched pathways of the m^{6}A-hypomethylated and differentially upregulated genes in sgM14-hWA versus sgNTC-hWA cells. **k** Schematic depicting experimental strategy to knockdown *METTL14* in the differentiated hWA cells for m^{6}A- and RNA-seq (Created with BioRender.com). **l** Venn diagram representation of the intersection of the m^{6}A-hypomethylated and upregulated genes in siM14-hWA versus siNTC-hWA cells. Wildtype hWA cells were fully differentiated and transfected with siNTC or siM14 to knock down *METTL14* in the mature hWA cells. Statistical analyses were performed using the Benjamin-Hochberg procedure and genes were filtered for $p < 0.01$ and FDR < 0.05, respectively. **m** Top 10 enriched pathways of the m^{6}A-hypomethylated and upregulated genes in siM14-hWA versus siNTC-hWA cells. **n** Coverage plots of m^{6}A peaks in *TRAIL* (**l**), *TNFSF1R* (**m**), *RIP1K* (**n**), *CASP7* (**o**), *DFFA* (**p**) genes in sgM14-hWA versus sgNTC-hWA cells. Plotted coverages are the median of the n replicates presented. **o**, **p** Heatmaps of genes related to TNFα and apoptosis signaling pathways (**o**) and prostaglandins synthesis and regulation pathway (**p**) (filtered by FDR < 0.05) in sgM14-hBAcells versus sgNTC-hBA cells, or sgM14-hWA cells versus sgNTC-hWA cells. **q** A proposed model for the molecular mechanism of action that METTL14-mediated m^{6}A installation selectively destabilizes transcripts in brown (left panel) and white adipocytes (right panel). *p*-values of pathway enrichment analysis were calculated according to the hypergeometric test based on the number of physical entities present in both the pre-defined set and user-specified list of physical entities (**e**–**h**, **j**, **m**). Source data are provided as a Source Data file.

usually inhibits lipolysis via Akt activation[35,36], yet the authors suggested enhanced insulin sensitivity and lipolysis synergy, creating interpretive challenges. In contrast, our study reveals the downregulation of lipolysis pathways in the Mettl14$^{fl/fl}$-Adipoq^{cre} iWAT (Fig. 5i), aligning with a consistent decrease in circulating FFAs (Fig. 7i). *Mettl14* deficiency in WAT induces insulin resistance in a tissue-autonomous manner. This, in turn, leads to severe peripheral insulin resistance through adipocyte apoptosis-induced triglyceride spillover and systemic inflammation. Nevertheless, other factors, including diets, and differences in microbiome composition secondary to housing conditions should be considered when interpreting the discrepancies of the two studies.

Our study identifies specific transcripts by which METTL14 negatively governs the secretory function within BAT and positively regulates the lipid sequestration capability within WAT in an m^{6}A-dependent manner. This cell-type-specific regulation by METTL14-mediated m^{6}A can be attributed to various factors. The level of m^{6}A modification depends on the expression and abundance of m^{6}A regulators including METTL14 and METTL3, the intrinsic preference of METTL3/METTL14 methyltransferase for specific nucleotide sequences, and the extrinsic regulation of methyltransferase complex activity by transcription factors, RNA-binding proteins (PBPs), RNA polymerases, histone modification, or posttranslational modifications[37–39].

The cell-type specificity of m^{6}A modifications is highlighted by the differential expression and protein abundance of METTL14 across various cell types. Specifically, under physiological conditions, METTL14 exhibits significantly lower protein levels of iBAT and hBAs compared to iWAT and hWAs, respectively (Supplementary Fig. 1f–h). Despite METTL3 being the enzyme with catalytic activity, its function is critically dependent on forming a complex with METTL14[40]. Therefore, the observed variability in METTL14 abundance may lead to differences in the activity of the m^{6}A writer complex and substrate availability. This, in turn, could result in distinct m^{6}A target preferences, influencing the physiological functions of brown versus white adipose tissues.

It is evident that genes associated with prostaglandin synthesis and regulation, as well as thermogenesis pathways, demonstrate robust expression within brown adipocytes. Conversely, genes linked to the TNF signaling pathway, apoptosis, and lipid and atherosclerosis pathways exhibit pronounced expression in white adipocytes. METTL14 is likely to preferentially recognize transcripts that are relevant and essential for the specific functions of each cell type. Thus, the selective targeting of transcripts by METTL14 reflects the unique inherent gene expression patterns and cellular functions in diverse cells and tissues, such as BAT and WAT.

Besides, previous reports indicate that certain transcription factors can direct the methyltransferase complex to specific RNA transcripts at their genomic sites[41,42]. For example, RNA-binding proteins such as TARBP2 can guide the complex to their bound transcripts[43]. RNA-binding motif protein 33 (RBM33) recruits ALKBH5 to its m^{6}A-marked substrate and activates ALKBH5 demethylase activity through the removal of its SUMOylation[44]. We have reported that both METTL3 and METTL14 activity is sensitive to the redox state of cells[38]. Slowed transcription rates may boost m^{6}A deposition by aiding co-transcriptional recruitment of the methyltransferase complex[45]. Additionally, H3K36me3 histone modification could aid complex recruitment to chromatin, promoting RNA methylation[46]. Depletion of METTL14 may trigger compensatory changes in other m^{6}A regulators, reshaping the overall m^{6}A modification landscape, and impacting the ability of METTL14 for transcript binding and target selection. These factors contribute to context-dependent m^{6}A modifications across cell types and tissues, necessitating further research to unravel the diverse physiological and pathological implications of this writer. Taken together, these findings collectively illuminate the mechanisms through which diverse biological cues can influence METTL14-mediated m^{6}A deposition, resulting in varied downstream effects on cell-type-specific gene expression patterns and phenotypic outcomes.

We acknowledge the limitations of our study. While our study provided evidence supporting the critical role of METTL14 in maintaining mature white adipocyte function, one limitation is the absence of in vivo data specifically pertaining to *Mettl14* deficiency exclusively in mature white adipocytes. Thus, future investigations utilizing adipose-specific knockout by local injection of AAV-shRNA-*Mettl14* are necessary. Besides, future studies are warranted to pinpoint the precise mechanism by which METTL14 selectively targets distinct genes in BAT or WAT, to define molecular interactions and regulatory networks involved in m^{6}A-regulated gene regulation in specific adipose tissue depots. These investigations would contribute to further understanding of the cell-type-specific functions of METTL14-mediated m^{6}A mRNA modification and shed light on the intricacies of adipose tissue metabolism and physiology. Moreover, our study does not rule out the potential involvement of other m^{6}A readers, such as YTHDC1/2 and IGF2BP1/2/3, or the impact of their differential expression on METTL14-mediated m^{6}A modifications in WAT versus BAT. This

highlights the need for further investigation into their roles. Additionally, while we have speculated regarding the discrepancies in transcriptomes between M14$^{fl/fl}$-Adipoq^{cre}-iBAT and M14$^{fl/fl}$-Ucp1^{cre}-iBAT, and discussed the differences between our findings and those reported by Kang et al. the precise underlying causal factors remain unclear. These unresolved aspects underscore the necessity for additional research to further elucidate the mechanisms involved.

Given the realization of the therapeutic potential of targeting m^{6}A regulators for numerous health conditions[47–49], we propose a precision targeting approach in a cell-type-specific fashion. This innovative therapeutic approach holds promise for shaping the future landscape of intervening in metabolic disorders.

Methods

Experimental model and human subject details

Ethical statement. Our research complies with all relevant ethical regulations. All animal protocols were approved by the Institutional Animal Care and Use Committee (IACUC) of the Joslin Diabetes Center following National Institutes of Health (NIH) guidelines.

Fig. 7 | *METTL14* deficiency promotes apoptosis in mouse and human white adipocytes. a Representative pictures of immunofluorescence staining of apoptotic nuclei (TUNEL-stain, green), adipocytes (PERILIPIN-stain, red), and nuclei (DAPI, blue) in eWAT and iWAT sections collected from male $M14^{fl/fl}$ and $M14^{fl/fl}$-$Adipoq^{cre}$ mice fed with HFD ($n = 7$/group) (scale bar, 50 μm; insert, 2× magnification). **b**, **c** Quantification of TUNEL-positive nuclei as a percentage of total nuclei in eWAT (**b**) and iWAT (**c**) of male $M14^{fl/fl}$ and $M14^{fl/fl}$-$Adipoq^{cre}$ mice fed with HFD ($n = 7$/group). **d** qRT-PCR analysis of the indicated mRNAs in the iWAT of male $M14^{fl/fl}$ and $M14^{fl/fl}$-$Adipoq^{cre}$ mice ($n = 10$/group). mRNA levels were normalized to *Actb*. **e**, **f** Western blot analysis (**e**) and quantification (**f**) of the indicated proteins in the iWAT of male $M14^{fl/fl}$ and $M14^{fl/fl}$-$Adipoq^{cre}$ mice. VINCULIN was used as a loading control ($n = 5$/group). **g**, **h** ELISA analysis of free fatty acid (FFA) (**g**, $n = 10$ for $M14^{fl/fl}$, and $n = 11$ for $M14^{fl/fl}$-$Adipoq^{cre}$) and triglyceride (TG) (**h**, $n = 10$/group) levels in the serum of male $M14^{fl/fl}$ and $M14^{fl/fl}$-$Adipoq^{cre}$ mice on HFD. **i** ELISA analysis of triglyceride (TG) levels in the liver and muscle of male $M14^{fl/fl}$ and $M14^{fl/fl}$-$Adipoq^{cre}$ mice on HFD (left panels) and iBAT removed cohort on CD (right panels) ($n = 6$/group for liver and muscle from HFD-fed mice, and liver from iBAT removed mice; $n = 5$ for muscle from iBAT removed $M14^{fl/fl}$ mice, and $n = 6$ for iBAT from iBAT removed $M14^{fl/fl}$-$Adipoq^{cre}$ mice). **j** qRT-PCR analysis of the indicated mRNAs in the differentiated sgNTC-hWA and sgM14-hWA cells. mRNA levels were normalized to *ACTINB* mRNA ($n = 4$/group). **k** Western blot analysis of the indicated proteins in the differentiated sgNTC-hWA and sgM14-hWA cells. TUBULIN was used as a loading control ($n = 3$/group). **l** ELISA analysis of FFA (upper panels, $n = 5$ for sgNTC, and $n = 4$ for sgM14) and TG (lower panels, $n = 7$ for sgNTC, and $n = 5$ for sgM14) levels in the culture medium of differentiated sgNTC-hWAs and sgM14-hWA cells. **m** A proposed model illustrating the mechanism of systemic insulin resistance induced by WAT-apoptosis in the $M14^{fl/fl}$-$Adipoq^{cre}$ mouse model (Created with BioRender.com). All samples in each panel are biologically independent. Data are presented as means ± SEM from two or three independent experiments by Two-tailed unpaired t-tests (**b**–**d**, **f**–**i**, **j**, **l**). Source data are provided as a Source Data file.

Mouse models and treatment. $Mettl14^{fl/fl}$ mice on a C57BL/6 N background[21,50] were crossed with $Ucp1^{cre}$ strain (stock no.024670, the Jackson Laboratory) or $Adipoq^{cre}$ strain (stock no.028020, the Jackson Laboratory) not harboring the nicotinamide nucleotide transhydrogenase (Nnt) mutation, were used to generate the knockouts. $M14^{fl/fl}$, $M14^{fl/fl}$-$Ucp1^{cre}$, and $M14^{fl/fl}$-$Adipoq^{cre}$ mice were fed with a chow diet (cat. no. 5020, LabDiet). For studies on diet-induced obesity and long-term insulin resistance, $M14^{fl/fl}$, $M14^{fl/fl}$-$Ucp1^{cre}$, and $M14^{fl/fl}$-$Adipoq^{cre}$ mice were fed either 60% fat HFD (D12492, Research Diets, New Brunswick, NJ), or sucrose matched 10% fat LFD (D12492J, Research Diets, New Brunswick, NJ) for 14–20 weeks, starting at 6 weeks of age. All mice were kept in a temperature- and humidity-controlled room (23 °C, 30%) on a 12 h light/dark cycle (lights on 06:30 am; off 06:30 pm) unless indicated with free access to food and water. To assess tissue-specific insulin sensitivity, mice were fasted for 16 h. Anesthesia was induced by intraperitoneal injection of 250 mg/kg tribromoethanol (AVERTIN®). Mice were monitored until they were fully anesthetized, as confirmed by the absence of foot withdrawal reflexes, followed by a 1 U injection of insulin (Humalog U-100) directly into the *vena cava*, as previously described[19]. Tissues were harvested at the indicated time points as shown in Fig. 3a.

Six-week-old *ob*+ and *ob/ob* ($B6.Cg\text{-}Lep^{ob}/J$) male mice were purchased from The Jackson Laboratory and maintained on a CD for 6 weeks. Intraperitoneal insulin tolerance tests (IPITT) and intraperitoneal glucose tolerance test (IPGTT) were performed at either 11 weeks or 12 weeks of age. Adipose tissues were collected for the assessment of m^6A regulator protein abundance by Western blot analysis. Additionally, serum samples were collected at 12 weeks of age for insulin measurement.

db+ and *db/db* (BKS.Cg-Dock7<m > +/+Lepr<db > /J) mice were purchased from The Jackson Laboratory (Strain 000642). Adipose tissues were collected for the assessment of m^6A regulator protein abundance by Western blot analysis. Additionally, serum samples were collected at 10 weeks of age for insulin measurement.

Acute cold exposure. For studies on cold tolerance tests, $M14^{fl/fl}$, $M14^{fl/fl}$-$Ucp1^{cre}$, and $M14^{fl/fl}$-$Adipoq^{cre}$ mice were caged individually at an ambient temperature of 5 °C for 1 to 6 h in temperature-controlled diurnal incubators (Caron Products and Services) with *ad lib* access to water and food. Rectal temperature was measured at 1 h intervals for core body temperature.

iBAT removal surgery. For assessing the contribution of BAT in systemic insulin sensitivity, IPITT was performed with $M14^{fl/fl}$ and $M14^{fl/fl}$-$Adipoq^{cre}$ mice on CD before and after iBAT removal. iBAT removal was adapted from a previous study[51], during the surgery, mice were anesthetized using isoflurane, a small incision was made in the interscapular depot, Sultzer's vein was ligated to prevent breeding, and interscapular brown adipose tissue was gently dissected from surrounding muscle. The incision was sutured to close the wound. IPITT was performed 10 days post-surgery, and tissues were harvested at 31 days post-surgery.

Rescue experiment with AAV8 vectors. To achieve specific knockdown of *Trail* or *Tnfr1* in the iWAT of $M14^{fl/fl}$-$Adipoq^{cre}$ mice, four groups of mice were included: $M14^{fl/fl}$ mice received injections of AAV8-eGFP (referred to as AAV-scramble), while $M14^{fl/fl}$-$Adipoq^{cre}$ mice were randomly divided into three groups. One group received AAV8-eGFP (AAV-scramble, VectorBuilder, CAT#: VB010000-0023jze), while the other two groups were injected with AAV8 vectors designed to knock down either *Trail* (AAV8-sh*Trail*, VectorBuilder, CAT#: VB230914-1451swv) or *Tnfr1* (AAV8-shTnfr1, VectorBuilder, CAT#: VB230914-1449xhd). The procedure for iWAT-specific AAV injection using Hamilton syringes was previously detailed in ref. 51. Briefly, each mouse received a total of 30 μL of AAV (10^13 genome copies/mL (GC/mL)), administered into the iWAT with 15 μL of AAV distributed across three injection sites within each iWAT. Knockdown of each gene was verified by WB. IPITT was conducted at 5 weeks post-AAV injection, while IPGTT was performed at 6 weeks post-AAV injection. At the end of the experiment, tissues were collected after *vena cava* insulin injection as described before in mouse models and treatment section.

Human cohort. A cohort of 72 individuals was selected from the Leipzig obesity biobank to encompass a diverse spectrum of parameters related to glucose metabolism. Subcutaneous and visceral white adipose tissues were collected from this cohort to analyze METTL14 protein abundance. The cohort consisted of 40 women and 32 men with obesity (sex was defined based on the biological attribute), exhibiting a range of BMI spanning from 20.5 to 54.5 kg/m^2. Based on BMI and homeostatic model assessment of insulin resistance (HOMA-IR > 2.9) scores, the cohort was categorized into four subgroups: lean-insulin sensitive, lean-insulin resistant, individuals with obesity who are insulin-sensitive, and individuals with obesity who are insulin-resistant. Noteworthy, patients with type 2 diabetes were newly diagnosed and did not receive antidiabetic medication. Detailed patient information can be found in Supplementary Table 1. The acquisition of human biomaterial, serum analyses, and phenotypic assessments was conducted as previously described in ref. 52. The human study was approved by University of Leipzig's ethics committee (approval numbers: 159-12-21052012 and 017-12-23012012), and informed written consent was obtained from all participants.

Human brown and white adipocyte culture and differentiation Immortalized human preadipocytes[20] were cultured in high-glucose DMEM supplemented with 10% FBS. Upon reaching

https://doi.org/10.1038/s41467-024-55694-w

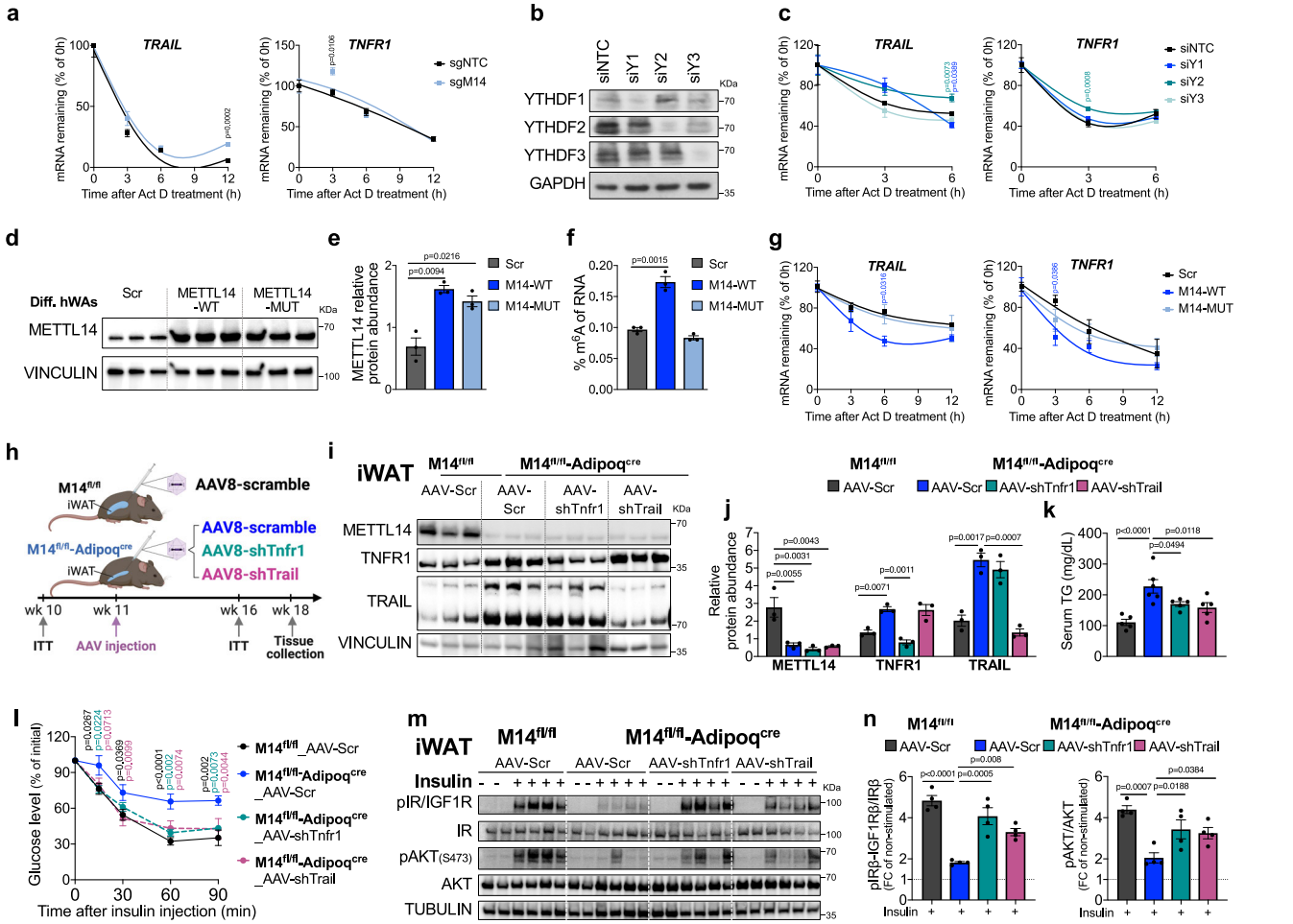

Fig. 8 | METTL14-mediated m^{6}A promotes decay of *TNFR1* and *TRAIL* in a YTHDF2/3 dependent manner in white adipocytes. a qRT-PCR analysis of the *TRAIL* and *TNFR1* mRNA in differentiated sgNTC-hWA and sgM14-hWA cells after a time-course treatment with 100 μg/mL Actinomycin D (Act D). mRNA levels were normalized to *ACTINB* mRNA ($n = 3$). **b** Representative Western blot of YTHDF1, YTHDF2, and YTHDF3 protein levels in differentiated wildtype hWA cells transfected with siNTC, siYTHDF1, siYTHDF2, or siYTHDF3 siRNA. GAPDH was used as a loading control ($n = 3$). **c** qRT-PCR analysis of *TRAIL* and *TNFR1* mRNA in differentiated wildtype hWA cells transfected with siNTC, siYTHDF1, siYTHDF2, or siYTHDF3 siRNA following a time-course treatment 100 μg/mL Act D. *TRAIL* and *TNFR1* mRNA levels were normalized to *ACTIN* ($n = 4$). The *p*-value indicates the significance of differences between any group and the siNTC group. **d**, **e** Western blot analysis (**d**) and quantification (**e**) of METTL14 protein abundance in the differentiated hWA cells transfected with scramble, wild-type METTL14 (METTL14-WT), or mutated METTL14 at R298 (METTL14-MUT) plasmid ($n = 3$/group). **f** Relative m^{6}A levels in the differentiated hWA cells transfected with scramble, wild-type METTL14-WT, or METTL14-MUT plasmid ($n = 3$/group). **g** qRT-PCR analysis of *TRAIL* and *TNFR1* mRNA in the differentiated hWA cells transfected with scramble, wild-type METTL14-WT, or METTL14-MUT plasmid after a time-course treatment with 100 μg/mL Actinomycin D (Act D). *TRAIL* and *TNFR1* mRNA levels were normalized to *ACTINB* mRNA ($n = 3$). The p-value indicates the significance of differences between any group and the Scr group. **h** Scheme of experimental approach depicting M14$^{fl/fl}$ mice receiving AAV8 eGFP (AAV-scramble), M14$^{fl/fl}$-Adipoq^{cre} mice receiving AAV8 eGFP, M14$^{fl/fl}$-Adipoq^{cre} mice receiving AAV8 knocking down Tnfr1 (AAV-shTnfr1), and M14$^{fl/fl}$-Adipoq^{cre} mice receiving AAV8 knocking down Trail (AAV-shTrail) (Created with BioRender.com). **i**, **j** Representative Western blot analysis (**i**) and quantification (**j**) of METTL14, TNFR1, and TRAIL protein levels in iWAT of the AAV-injected mice ($n = 3$). **k** Serum TG levels measured by ELISA assays ($n = 5$–6/group). **l** Intraperitoneal insulin tolerance tests of mice injected with AAVs ($n = 7$ for M14$^{fl/fl}$-AAV-Scr group; $n = 5$ for M14$^{fl/fl}$-Adipoq^{cre}_AAV-Scr group, $n = 7$ for M14$^{fl/fl}$-Adipoq^{cre}_AAV-shTnfr1 group, $n = 8$ for M14$^{fl/fl}$-Adipoq^{cre}_AAV-shTrail group,). The *p*-value indicates the significance of differences between any group and the M14$^{fl/fl}$-Adipoq^{cre}_AAV-Scr group. **m**, **n** Western blot analysis (**m**) and quantification (**n**) of pIRβ/IGF1Rβ and pAKT$_{S473}$ in iWAT 5-week post-AAV injections, followed by injection of 1U of insulin via the *vena cava* (n = 2 for non-stimulated groups; $n = 4$ for insulin-stimulated groups). The *p*-value indicates the significance of differences between any group and the M14$^{fl/fl}$-Adipoq^{cre}_AAV-Scr group. All samples in each panel are biologically independent. Data are presented as means ± SEM from two or three independent experiments by Two-tailed unpaired t-test (**a**), One-way ANOVA (**c**, **g**), and Two-way ANOVA (**e**, **f**, **j**, **k**, **l**, **n**). Source data are provided as a Source Data file.

confluence, brown or white adipocyte differentiation was initiated by treatment with induction medium, which consisted of DMEM high-glucose medium with 10% FBS, 33 μM biotin, 17 μM pantothenate, 0.5 μM human insulin, 500 μM IBMX, 2 nM T3, 0.1 μM dexamethasone, and 30 μM indomethacin, for a duration of 21 or 18 days, respectively. Following complete differentiation, cells were washed with PBS, and both RNA and protein were extracted for conducting qRT-PCR and western blot analyses, respectively.

Knock-out experiments. To establish stable *METTL14* knockouts in hBA or hWA preadipocytes, three different Edit-R All-in-one Lentiviral human *METTL14* single guide RNAs (sgM14) and a Non-targeting control single guide RNA (sgNTC) obtained from Horizon Discovery were utilized (Dharmacon, VSGH11940-15EG57721). After lentiviral transduction, the hBA or hWA preadipocytes were subjected to puromycin treatment for 6 days to select and establish stable M14 knockout lines for subsequent adipocyte differentiation and functional experiments. The knockouts were confirmed using western blot analyses.

Knock-down experiments. For the transient knockdown of *METTL14*, *YTHDF1*, *YTHDF2*, *YTHDF3*, *TRAIL*, *DR5*, *TNFα*, or *TNFR1* in differentiated hWA cells, Lipofectamine RNAiMAX Reagent (Invitrogen) was used to deliver siRNA complexes (Dharmacon) at a final concentration of 15 nmol/L siRNA, with an RNAiMAX:siRNA ratio of 4:1. The specific siRNAs used were as follows: ON-TARGETplus Non-Targeting Control Pool D-001810-10-05, ON-TARGETplus Human *METTL14* siRNA (L-014169-02-0020), ON-TARGETplus Human *YTHDF1* siRNA (L-018095-02-0005), ON-TARGETplus Human *YTHDF2* siRNA (L-021009-02-0005), and ON-TARGETplus Human *YTHDF*3 siRNA (L-017080-01-0005), ON-TARGETplus Human *TNFSF10* siRNA (L-011524-00-0005), ON-TARGETplus Human *TNFRSF10B* siRNA (L-004448-00-0005), ON-TARGETplus Human TNF siRNA (L-010546-00-0005), ON-TARGETplus Human *TNFRSF1A* siRNA (L-005197-00-0005). All the experiments were conducted on the knockdown cells 72 h post-transfection.

Establishment of overexpression of wildtype-METTL14 or mutant-METTL14 (R298P). To achieve stable overexpression of wildtype-METTL14 or mutant-METTL14 (R298P) in differentiated hWAs, scramble, pCDH-METTL14-WT (Addgene plasmid # 141112; http://n2t.net/addgene:141112; RRID: Addgene_141112), or PCDH-METTL14-R298P (Addgene plasmid # 141113; RRID: Addgene_141113)[5] plasmid was transfected into the cells using Lipofectamine 3000 Transfection Reagent (Invitrogen L3000015) (DNA: Lipofectamine = 1:3 ratio). Plasmids were gifts from Jianjun Chen[5].

Cell treatments

Actinomycin D treatment. Differentiated sgNTC-hWA and sgM14-hWA cells, or Scramble-, METTL14-WT-, and METTL14-Mut-hWA cells were treated with 100 μg/mL Actinomycin D (Thermo Fisher) or DMSO for 0, 3, 6 or 12 h. For siNTC-, siYTHDF1-, siYTHDF2-, and siYTHDF3-hWA cells, treatment with Actinomycin D or DMSO was conducted for 0, 3, and 6 h.

Method Details

Intraperitoneal glucose and insulin tolerance tests. For the intraperitoneal glucose tolerance test, the mice were subjected to an overnight fast and then received an intraperitoneal injection of glucose (2 g/kg body weight) as reported previously[53]. Blood glucose levels were measured at baseline (0 min) and 15, 30, 45, 60, 90, and 120 minutes after the injection using Contour next EZ glucometer.

For the intraperitoneal insulin tolerance test, the mice were fasted for 6 h and then injected intraperitoneally with 1 U/kg insulin for males and 0.7 U/kg insulin for females. Blood glucose levels were measured at baseline (0 min) and 15, 30, 45, 60, and 90 min after the injection using Contour next EZ glucometer.

Food intake, energy expenditure, and body composition measurements. For indirect calorimetry, the mice were individually housed in metabolic cages within a Comprehensive Lab Animal Monitoring System (CLAMS) set at room temperature. Following a 12-hour acclimation period, the animals were exposed to acute cold exposure as previously described in the acute cold exposure section. Subsequently, the mice were continuously monitored for 72 hours to obtain measurements of energy expenditure, volume of oxygen consumption (VO_2), and volume of carbon dioxide production (VCO_2). Body composition, including total mass, fat mass, and lean mass, was assessed using a Dual-energy X-ray absorptiometry (DEXA) scan.

RNA isolation and quantitative RT-PCR. Total RNA of high quality and a minimum length of 200 nucleotides was isolated using Trizol reagent (Invitrogen), adhering to the guidelines provided by the manufacturer. Post-extraction, the aqueous layer was mixed in equal parts with RNase-free 70% ethanol and applied to columns from the Qiagen RNeasy Mini Kit (Qiagen) according to the manufacturer's protocol. Quality and quantity assessments of the extracted RNA were performed using a Nanodrop 1000 spectrophotometer. For reverse transcription, we utilized the High Capacity cDNA Synthesis Kit from Applied Biosciences. cDNA analysis was conducted using the ABI 7900HT Fast Real-Time PCR system (Applied Biosciences), with gene expression levels quantified by the comparative ΔΔCt method. Normalization of data was carried out against housekeeping genes. Primer sequences used for amplification are listed in Supplementary Table 2.

Western blots and molecular analyses. Total proteins were extracted from tissue and cell line lysates using M-PER (for cell samples) or RIPA (for tissue samples) protein extraction reagent (Thermo Fisher) supplemented with proteinase and phosphatase inhibitors (Sigma) following the standard protocol. The protein concentrations were determined using the BCA assay, and standard western immunoblotting procedures were employed to analyze the proteins. Chemiluminescent substrate ECL (Thermo Fisher) was used for blot development, and ImageJ software was utilized for quantification of the results.

m^{6}A immunoprecipitation and sequencing. To characterize the m^{6}A methylome, m^{6}A-seq (m^{6}A-MeRIP-seq) was employed as described by a previous study[24]. Approximately 1 μg of mRNAs was extracted from total RNA using the Dynabeads mRNA DIRECT purification kit from Thermo Fisher. Subsequently, the mRNA was adjusted to a concentration of approximately 10 ng/μl in a total volume of 100 μl and then fragmented using a Bioruptor ultrasonicator (Diagenode) with a cycling pattern of 30 s on and 30 s off for a total of 30 cycles. A portion of each sample (5 μl) was preserved as the 'input' control.

For m^{6}A immunoprecipitation (m^{6}A-IP) and library preparation, the EpiMark N^6-Methyladenosine enrichment kit from NEB was employed. The RNA eluted from m^{6}A-IP and the 'input' samples were used for library generation utilizing the TruSeq stranded mRNA sample preparation kit from Illumina. Subsequent sequencing was performed on an Illumina HiSeq 6000 platform following the manufacturer's guidelines.

Differential gene expression analysis for RNA-seq

As reported previously[21], the input library of m^{6}A seq is essentially an mRNA sequencing library. Thus, we performed gene-level differential expression analysis using the input libraries. Raw reads were trimmed using Cutadapt (4.2) and aligned to the hg38 genome (GRCh38.107) and mm10 (GRCm38.102) using HISAT2 (2.2.1)[54] and SAMtools (1.16.1). Aligned sequencing reads were analyzed using RADAR (0.2.4)[55]. Then we perform differential gene expression (DGE) analysis of count data using the R package DESeq2 (1.36.0)[56]. We used a cut-off FDR < 0.05 to select differentially expressed transcripts for pathway and gene ontology enrichment analyses. ConsensusPathDB[57] and the "Metascape"[58] online tools were used to perform enrichment analysis.

Differential methylation analysis for m^{6}A-seq

Using the R package RADAR[55], approximately 25 million single-end 100-bp reads were generated for each sample. Counts were normalized for library size and IP counts were adjusted for expression level by the gene-level read counts of input libraries. Bins with average IP-adjusted counts lower than 10 in both control and M14^{KO} groups were removed. Then bins that were not enriched in IP were also filtered out. To consider the pairing of m^{6}A IP and input, we use the normalized, expression-level-(i.e., input)-adjusted, and low-read-count-filtered IP counts. Using Wald tests, we tested for significant effects of M14 knockout on the m^{6}A enrichment/depletion. We adjusted for multiple testing using the Benjamini-Hochberg false discovery rate (FDR) controlling procedure and used FDR < 0.1 and logFC > 0.5, in line with the parameters recommended by the RADAR workflow in our previous studies for differential methylation analysis.

m^{6}A ELISA

m^{6}A level in total RNA (200 ng) extracted from differentiated hWAs (Scramble, M14-WT, and M14-MUT) was quantified by EpiQuik™ RNA Methylation Quantification kit (Colorimetric) according to the manufacturer's instructions. Relative m^{6}A RNA methylation status is calculated by the following formula:

*m^{6}A% = ((sample OD value - negative control OD value) / amount of input sample)/(positive control OD value - negative control OD value) * 100%*

Hematoxylin and Eosin and immunofluorescence staining

For Hematoxylin and Eosin (H&E) staining, mouse tissues were fixed in 4% paraformaldehyde (PFA) at 4 °C overnight, followed by 70% ethanol dehydration and paraffin embedding. Multiple 5 µm sections were prepared and subjected to H&E staining following standard procedures. Imaging was conducted using a Zeiss AxioImager M1 microscope. For immunostaining, paraffin-embedded tissues were deparaffinized in xylene and rehydrated. Heat-induced epitope retrieval was performed using a target retrieval solution (Dako). Tissues were blocked with PBS containing 10% goat serum and 0.1% Tween 20 for 60 min. Following PBS washing, slides of iWAT and eWAT tissues were stained with TUNEL (Sigma s7110), PERILIPIN (CST #9349S), and DAPI staining according to the manufacturer's instructions.

Measurement of blood parameters

To measure insulin, adiponectin, and leptin levels, serum was collected via cardiac puncture following the anesthesia of the mice. The concentrations of insulin (Crystal Chem, #90082), adiponectin (Crystal Chem, #80569), and leptin (Crystal Chem, #90030) were determined using enzyme-linked immunosorbent assay (ELISA) kits, following the manufacturer's protocols.

Free fatty acid and triglyceride measurements

For plasma samples, FFAs (Abcam ab65341) and triglyceride (TG) (Promega Triglyceride-Glo™ J3160) concentrations were measured using according to the manufacturer's instructions.To measure the TG levels in liver and muscle tissues, the tissues were homogenized and centrifuged, and the supernatant was collected. The triglyceride content was then measured using colorimetric kits, following the manufacturer's protocol (Stanbio Triglycerides LiquiColor, 2100430).

In vitro glucose uptake assays

Approximately 30,000 cells were seeded per well in a 96-well plate. Once the cells reached 80–90% confluency, differentiation was induced following established protocols. After differentiation, the cells were treated with 100 nM insulin for 15 min. Glucose uptake was then measured using the Glucose Uptake-Glo™ Assay kit (Promega, J1341), according to the manufacturer's instructions.

Seahorse mitochondrial stress test and glycolytic stress test

Approximately 50,000 cells were seeded per well in a Seahorse XF24 cell culture microplate. Fully differentiated hWAs or hBAs were pretreated with or without 1 µM CL-316,243 for 4 hours. Following this, the Seahorse XF Cell Mito Stress Test (Agilent, 103015-100) or Seahorse XF Glycolysis Stress Test (Agilent, 103020-100) was performed using the XFe24 Analyzer according to the manufacturer's protocol. A BSA assay was conducted to quantify the total protein abundance in each well, which was then used to normalize the OCR and ECAR data.

Quantification and statistical analysis

The presented data is represented as mean values ± standard error of the mean (SEM.), and statistical significance was assessed using either a Two-tailed Student's t-test, a One-way analysis of variance (ANOVA), or a Two-way ANOVA. Details of the applied statistical tests and corresponding sample sizes ('n') are provided in the respective figure legends. In the case of in vitro experiments, 'n' indicates the number of independent experimental repetitions. In animal experiments and tissue analyses, 'n' corresponds to the number of mice utilized per genotype or condition. For human white adipose tissue, 'n' signifies the number of donors included within each group.

Correlations between METTL14 protein abundance of visceral and subcutaneous WATs of the human cohort were calculated using Graphic Prism v.9 software, based on the Spearman correlation coefficient, and a confidence interval of 0.95. Figures have been generated using GraphPad Prism9, and BioRender.com.

Reporting summary

Further information on research design is available in the Nature Portfolio Reporting Summary linked to this article.

Data availability

m^{6}A-sequencing and RNA-sequencing datasets from mouse brown adipose tissue, white adipose tissue, differentiated human brown adipocytes, and differentiated human white adipocytes have been deposited with the National Center for Biotechnology Information Gene Expression Omnibus under accession code GSE250137. Source data are provided in this paper. All data supporting the findings described in this manuscript are available in the article and in the Supplementary Information and from the corresponding author upon request. Source data are provided with this paper.

References

1. Zhao, B. S., Roundtree, I. A. & He, C. Post-transcriptional gene regulation by mRNA modifications. *Nat Rev Mol Cell Biol.* **18**, 31–42 (2017).
2. Zaccara, S., Ries, R. J. & Jaffrey, S. R. Reading, writing and erasing mRNA methylation. *Nat Rev Mol Cell Biol.* **20**, 608–624 (2019).
3. Yi, D. et al. METTL14 promotes the migration and invasion of breast cancer cells by modulating N6-methyladenosine and hsa-miR-146a-5p expression. *Oncol Rep.* **43**, 1375–1386 (2020).
4. Wang, M. et al. Upregulation of METTL14 mediates the elevation of PERP mRNA N(6) adenosine methylation promoting the growth and metastasis of pancreatic cancer. *Mol Cancer.* **19**, 130 (2020).
5. Weng, H. et al. METTL14 Inhibits Hematopoietic Stem/Progenitor Differentiation and Promotes Leukemogenesis via mRNA m(6)A Modification. *Cell Stem Cell.* **22**, 191–205.e9 (2018).
6. Yang, X. et al. METTL14 suppresses proliferation and metastasis of colorectal cancer by down-regulating oncogenic long non-coding RNA XIST. *Mol Cancer.* **19**, 46 (2020).
7. Gu, C. et al. Mettl14 inhibits bladder TIC self-renewal and bladder tumorigenesis through N(6)-methyladenosine of Notch1. *Mol Cancer.* **18**, 168 (2019).
8. Shi, H., Wei, J. & He, C. Where, When, and How: Context-Dependent Functions of RNA Methylation Writers, Readers, and Erasers. *Mol Cell.* **74**, 640–650 (2019).
9. Czech, M. P. Mechanisms of insulin resistance related to white, beige, and brown adipocytes. *Mol Metab.* **34**, 27–42 (2020).
10. Shamsi, F., Wang, C. H. & Tseng, Y. H. The evolving view of thermogenic adipocytes - ontogeny, niche and function. *Nat Rev Endocrinol.* **17**, 726–744 (2021).
11. Cohen, P. & Spiegelman, B. M. Cell biology of fat storage. *Mol Biol Cell.* **27**, 2523–2527 (2016).
12. Tsuji, T. & Tseng, Y. H. Adipose tissue-derived lipokines in metabolism. *Curr Opin Genet Dev.* **81**, 102089 (2023).
13. Alkhouri, N. et al. Adipocyte apoptosis, a link between obesity, insulin resistance, and hepatic steatosis. *J Biol Chem.* **285**, 3428–3438 (2010).
14. Kobayashi, M. et al. The RNA Methyltransferase Complex of WTAP, METTL3, and METTL14 Regulates Mitotic Clonal Expansion in

Adipogenesis. *Mol Cell Biol*. **15**, 38 https://doi.org/10.1128/mcb.00116-18 (2018).
15. Wang, Y. et al. METTL3 is essential for postnatal development of brown adipose tissue and energy expenditure in mice. *Nat Commun*. **11**, 1648 (2020).
16. Wang, Y. et al. WTAP regulates postnatal development of brown adipose tissue by stabilizing METTL3 in mice. *Life Metabolism*. **1**, 270–284 (2022).
17. Li, Y. et al. Rna M(6) a Methylation Regulates Glycolysis of Beige Fat and Contributes to Systemic Metabolic Homeostasis. *Adv Sci (Weinh)*. **5**,e2300436 (2023).
18. Xie, R. et al. Activation of METTL3 Promotes White Adipose Tissue Beiging and Combats Obesity. *Diabetes*. **72**, 1083–1094 (2023).
19. Xiao, L. et al. m(6)A mRNA methylation in brown fat regulates systemic insulin sensitivity via an inter-organ prostaglandin signaling axis independent of UCP1. *Cell Metab*. **4**, https://doi.org/10.1016/j.cmet.2024.08.006 (2024).
20. Xue, R. et al. Clonal analyses and gene profiling identify genetic biomarkers of the thermogenic potential of human brown and white preadipocytes. *Nat Med*. **21**, 760–768 (2015). Jul.
21. De Jesus, D. F. et al. m(6)A mRNA Methylation Regulates Human β-Cell Biology in Physiological States and in Type 2 Diabetes. *Nat Metab*. **1,** 765–774 (2019).
22. Eguchi, J. et al. Transcriptional control of adipose lipid handling by IRF4. *Cell Metab*. **13**, 249–259 (2011).
23. Kong, X. et al. IRF4 is a key thermogenic transcriptional partner of PGC-1α. *Cell*. **158**, 69–83 (2014).
24. Wang, X. et al. N6-methyladenosine-dependent regulation of messenger RNA stability. *Nature*. **505**, 117–120 (2014).
25. Kwok, K. H., Lam, K. S. & Xu, A. Heterogeneity of white adipose tissue: molecular basis and clinical implications. *Exp Mol Med*. **48**, e215 (2016).
26. Oguri, Y. & Kajimura, S. Cellular heterogeneity in brown adipose tissue. *J Clin Invest*. **130**, 65–67 (2020).
27. Shi, H. et al. YTHDF3 facilitates translation and decay of N(6)-methyladenosine-modified RNA. *Cell Res*. **27**, 315–328 (2017).
28. Matsumura, Y., Wei, F. Y. & Sakai, J. Epitranscriptomics in metabolic disease. *Nat Metab*. **5**, 370–384 (2023).
29. Kang, Q. et al. Adipose METTL14-Elicited N(6) -Methyladenosine Promotes Obesity, Insulin Resistance, and NAFLD Through Suppressing β Adrenergic Signaling and Lipolysis. *Adv. Sci. (Weinh)*:e2301645 (2023).
30. Kahraman, S. et al. m(6)A mRNA methylation by METTL14 regulates early pancreatic cell differentiation. *Embo J*. **25**, https://doi.org/10.1038/s44318-024-00213-2 (2024).
31. Kahn, B. B. & Flier, J. S. Obesity and insulin resistance. *J Clin Invest*. **106**, 473–481 (2000).
32. Morigny, P., Houssier, M., Mouisel, E. & Langin, D. Adipocyte lipolysis and insulin resistance. *Biochimie*. **125**, 259–266 (2016).
33. Inazumi, T. et al. Prostaglandin E(2)-EP4 Axis Promotes Lipolysis and Fibrosis in Adipose Tissue Leading to Ectopic Fat Deposition and Insulin Resistance. *Cell Rep*. **33**, 108265 (2020).
34. Grabner, G. F., Xie, H., Schweiger, M. & Zechner, R. Lipolysis: cellular mechanisms for lipid mobilization from fat stores. *Nat Metab*. **3**, 1445–1465 (2021).
35. Choi, S. M. et al. Insulin regulates adipocyte lipolysis via an Akt-independent signaling pathway. *Mol Cell Biol*. **30**, 5009–5020 (2010).
36. Santoro, A., McGraw, T. E. & Kahn, B. B. Insulin action in adipocytes, adipose remodeling, and systemic effects. *Cell Metab*. **33**, 748–757 (2021).
37. Xu, Z. et al. Crosstalk Between Histone and m(6)A Modifications and Emerging Roles of m(6)A RNA Methylation. *Front Genet*. **13**, 908289 (2022).
38. De Jesus, D. F. et al. Redox regulation of m(6)A methyltransferase METTL3 in β-cells controls the innate immune response in type 1 diabetes. *Nat Cell Biol*. **26**, 421–437 (2024).
39. Sun, H. L. et al. Stabilization of ERK-Phosphorylated METTL3 by USP5 Increases m(6)A Methylation. *Mol Cell*. **80**, 633–647.e7 (2020).
40. Wang, P., Doxtader, K. A. & Nam, Y. Structural basis for cooperative function of Mettl3 and Mettl14 methyltransferases. *Molecular cell*. **63**, 306–317 (2016).
41. Barbieri, I. et al. Promoter-bound METTL3 maintains myeloid leukaemia by m(6)A-dependent translation control. *Nature*. **552**, 126–131 (2017).
42. Bertero, A. et al. The SMAD2/3 interactome reveals that TGFβ controls m(6)A mRNA methylation in pluripotency. *Nature*. **555**, 256–259 (2018).
43. Fish, L. et al. Nuclear TARBP2 Drives Oncogenic Dysregulation of RNA Splicing and Decay. *Mol Cell*. **75**, 967–981.e9 (2019).
44. Yu, F. et al. RBM33 is a unique m6A RNA-binding protein that regulates ALKBH5 demethylase activity and substrate selectivity. *Molecular Cell*. **83**, 2003–2019. e6 (2023).
45. Slobodin, B. et al. Transcription Impacts the Efficiency of mRNA Translation via Co-transcriptional N6-adenosine Methylation. *Cell*. **169**, 326–337.e12 (2017).
46. Huang, H. et al. Histone H3 trimethylation at lysine 36 guides m(6)A RNA modification co-transcriptionally. *Nature*. **567**, 414–419 (2019).
47. Huang, H., Weng, H. & Chen, J. m(6)A Modification in Coding and Non-coding RNAs: Roles and Therapeutic Implications in Cancer. *Cancer Cell*. **37**, 270–288 (2020).
48. He, P. C. & He, C. m(6) A RNA methylation: from mechanisms to therapeutic potential. *Embo J*. **40**, e105977 (2021).
49. Ren, Y. et al. m(6) A mRNA methylation: Biological features, mechanisms, and therapeutic potentials in type 2 diabetes mellitus. *Obes Rev*. **21**, (2023); https://doi.org/10.1111/obr.13639
50. Kahraman, S. et al. m^{6}A mRNA Methylation Regulates Early Pancreatic β-Cell Differentiation. *bioRxiv*. 2023:2023.08.03.551675. https://doi.org/10.1101/2023.08.03.551675.
51. Tsuji, T., Zhang, Y., Tseng, Y. H. Generation of Brown Fat-Specific Knockout Mice Using a Combined Cre-LoxP, CRISPR-Cas9, and Adeno-Associated Virus Single-Guide RNA System. *J. Vis. Exp*. **24**, https://doi.org/10.3791/65083 (2023).
52. Klöting, N. et al. Insulin-sensitive obesity. *Am. J. Physiol. Endocrinol. Metab*. **299**, E506–E515 (2010).
53. Kulkarni, R. N. et al. Tissue-specific knockout of the insulin receptor in pancreatic beta cells creates an insulin secretory defect similar to that in type 2 diabetes. *Cell*. **96**, 329–339 (1999).
54. Kim, D., Langmead, B. & Salzberg, S. L. HISAT: a fast spliced aligner with low memory requirements. *Nat Methods*. **12**, 357–360 (2015).
55. Zhang, Z. et al. RADAR: differential analysis of MeRIP-seq data with a random effect model. *Genome Biol*. **20**, 294 (2019).
56. Love, M. I., Huber, W. & Anders, S. Moderated estimation of fold change and dispersion for RNA-seq data with DESeq2. *Genome Biol*. **15**, 550 (2014).
57. Herwig, R., Hardt, C., Lienhard, M. & Kamburov, A. Analyzing and interpreting genome data at the network level with ConsensusPathDB. *Nat. Protocols*. **11**, 1889–1907 (2016).
58. Zhou, Y. et al. Metascape provides a biologist-oriented resource for the analysis of systems-level datasets. *Nat Commun*. **10**, 1523 (2019).

Acknowledgements

The authors thank Joslin Animal Physiology Core, Joslin Bioinformatics Core (P30 DK36836). We thank Maureen Gannon PhD (Vanderbilt University), Philipp E Scherer PhD (UT Southwestern Medical Center), and Matthew Lynes PhD (University of Maine) for advice. This work is

supported by NIH grants R01 DK67536 (R.N.K.), RC2 DK139552 (R.N.K. and C.H.), UC4 DK116278 (R.N.K. and C.H.), and RM1 HG008935 (C.H.). R.N.K. acknowledges support from the Diabetes Research and Wellness Foundation Endowed Chair and C.H. is a Howard Hughes Medical Institute Investigator. D.F.D.J. acknowledges support by Mary K. Iacocca Junior Postdoctoral Fellowship, American Diabetes Association grant #7-21-PDF-140, and the NIH K99 Award DK135927. T.T. acknowledges support from the SUNSTAR Research Fellowship (Hiroo Kaneda Scholarship, Japan), the American Heart Association Grant 903968, and the Eleanor and Miles Shore Program Award from Harvard Medical School. Y.H.T. acknowledges support by NIH grants R01 DK102898 and R01 DK132469. Human validation studies were funded by the Deutsche Forschungsgemeinschaft (DFG, German Research Foundation) through CRC 1052, project number 209933838, subproject B1 to M.B.

Author contributions

L.X. and D.F.D.J. conceived the study, designed and performed experiments, analyzed the data, assembled figures, and wrote the manuscript. C.W.J. conducted RNA/m^{6}A-seq and m^{6}A LC-MS/MS experiments. J.B.W. assisted with RNA/m^{6}A-seq and m^{6}A LC-MS/MS experiments. J.H. performed immunohistochemistry. A.D.F. and V.S.G. assisted with animal experiments. T.T. performed the surgical removal of iBAT and assisted with AAV injection. S.Y.W. assisted with *METTL14* overexpression experiments. M.B. provided human white adipose tissues and edited the manuscript. Y.H.T. contributed to conceptual discussions and provided immortalized human white/brown pre-adipocytes and protocols for cell culture and differentiation. C.H. contributed to conceptual discussions and designed the experiments for RNA-seq and m^{6}A-seq. R.N.K. conceived the study, designed the experiments, supervised the project, and wrote the manuscript. All the authors have reviewed, commented on, and edited the manuscript.

Competing interests

R.N.K. is on the scientific advisory board of Novo Nordisk, Biomea and REDD. C.H. is a scientific founder and a member of the scientific advisory board of Accent Therapeutics. M.B. received honoraria as a consultant and speaker from Amgen, AstraZeneca, Bayer, Boehringer Ingelheim, Daiichi-Sankyo, Lilly, Novo Nordisk, Novartis, and Sanofi. The remaining authors have no conflicts of interest.

Additional information

Supplementary information The online version contains supplementary material available at https://doi.org/10.1038/s41467-024-55694-w.

Correspondence and requests for materials should be addressed to Rohit N. Kulkarni.

Peer review information *Nature Communications* thanks Søren Nielsen, Xinshou Ouyang and the other, anonymous, reviewer(s) for their contribution to the peer review of this work. A peer review file is available.